

Two Channels of Metal-Rich Compact Stellar System Formation: Starbursts Under High Ram Pressure vs. Tidal Stripping

Yuan Bian¹, Min Du^{1,*}, Victor P. Debattista², Dylan Nelson³, Mark A. Norris², Luis C. Ho^{4,5}, Shuai Lu¹, Renyue Cen^{6,7}, Shuo Ma¹, Chong Ge¹, Taotao Fang¹, and Hui Li⁸

¹*Department of Astronomy, Xiamen University, Xiamen, Fujian 361005, China*

²*Jeremiah Horrocks Institute, University of Central Lancashire, Preston PR1 2HE, UK*

³*Universität Heidelberg, Zentrum für Astronomie, ITA, Albert-Ueberle-Str. 2, 69120 Heidelberg, Germany*

⁴*Kavli Institute for Astronomy and Astrophysics, Peking University, Beijing 100871, China*

⁵*Department of Astronomy, School of Physics, Peking University, Beijing 100871, China*

⁶*Center for Cosmology and Computational Astrophysics, Institute for Advanced Study in Physics, Zhejiang University, Hangzhou 310027, China*

⁷*Institute of Astronomy, School of Physics, Zhejiang University, Hangzhou 310027, China*

⁸*Department of Astronomy, Tsinghua University, Haidian DS 100084, Beijing, China*

Most galaxies follow well-defined scaling relations of metallicity and stellar mass; however, some outliers at the low mass end of the observed galaxy population exhibit unusually high metallicity for their mass. Understanding how these objects get to be so metal-rich is vital for understanding the role of feedback in galaxy formation. Using the TNG50 simulation, we explore the origins of this phenomenon. We identify 227 metal-rich, Compact Stellar Systems (CSSs) that deviate significantly from this scaling relation. These CSSs are satellites located in the vicinity of massive host galaxies, with stellar masses ranging from $10^8 M_\odot$ to $10^{10} M_\odot$ (including six systems that are close analogs of the M31-M32 system). Contrary to the previously assumed scenario that such objects are predominantly products of tidal stripping, our results suggest a more prevalent role for ram pressure in their formation. Indeed, 76% (173) of these CSSs are formed through a burst of star formation occurring around the time of the first pericentric passage, typically at redshifts $z \lesssim 1$, aided by strong ram pressure and tidal forces. The high ram pressure, resulting from the CSSs' rapid motion near the halo center, facilitates metal enrichment, producing high-metallicity CSSs by confining the metal-rich gas from bursty star formation, which leads to distinct stellar populations characterized by enhanced metallicity as well as high α -abundance. Only the remaining 24% (54) of metal-rich CSSs are generated through the tidal stripping of massive progenitors. Our results further indicate that M32 is more likely to have formed through intense star formation events rather than through gradual, tidal stripping, thereby providing crucial insights into the nature of low mass, compact galaxy formation.

Over the past three decades, increasing numbers of compact stellar systems (CSSs) have been discovered. These intriguing objects occupy the parameter space between classical globular clusters (GC) and true galaxies. Based on previous studies, ultra-compact dwarf galaxies (UCDs) [1, 2, 3, 4, 5, 6, 7, 8] and compact elliptical galaxies (cEs) [9, 10, 11, 12, 13, 14], both fall under the broader category of CSSs, with UCDs extending above GCs mass ($M_* \gtrsim 10^6 - 10^8 M_\odot$) and cEs those objects at still higher masses ($\gtrsim 10^9 M_\odot$). Notably, some objects at the higher mass range ($M_* = 10^8 - 10^{10} M_\odot$) exhibit enhanced stellar metallicities, typically deviating by about 0.4 – 0.6 dex from the stellar mass-metallicity relation observed in ordinary dwarf galaxies of comparable mass [15], and more typical of galaxies with mass a factor of at least ten times higher.

A commonly invoked formation scenario for metal-rich CSSs is the heavy stripping of initially more massive galaxies [8, 13, 14, 16, 17, 18, 19]. CSSs caught in the act of formation and still embedded in tidal streams of stars from their disrupted progenitors provide some direct evidence

*E-mail: dumin@xmu.edu.cn

supporting this scenario [10, 20, 21, 22]. In this process, the least bound stars in the outer parts, which have lower metallicity, are preferentially stripped, leaving behind a metal-rich compact remnant. The resulting objects deviate from the mass–metallicity relation (see also ref.[10]) by virtue of the high metallicity of the bulge of their more massive progenitors. However, the extremely high metallicities of outliers in the mass–metallicity relation are only typical of the innermost regions ($\sim r_e/8$) of massive galaxies [23]. Thus, for instance, a Milky Way-sized progenitor would be necessary to generate M32 analogs if only tidal stripping were responsible for their formation. Yet, M31’s stellar halo is much less massive ($\sim 10^9 M_\odot$ level; see ref.[24, 25, 26, 27]), and no clear evidence of such a massive progenitor for M32 exists within M31 [28].

An alternative hypothesis posits the direct formation of metal-rich CSSs through starburst triggered within their host galaxy environments. Interactions with host galaxies can induce gas inflows towards the centers of gas-rich dwarfs [29]. Ref.[30] showed that the high ram pressure experienced during rapid passages near massive host galaxies promotes star formation through gas compression, increasing the stellar density in the central region, while also confining metals within the dwarf, leading to the rapid enrichment of new stellar populations. Independently, ref.[31] obtained similar results through wind tunnel experiments, also finding that ram pressure confines gas and metals to dwarf galaxies, which would otherwise have escaped their shallow potentials. We term this scenario the bursty star formation (BSF) scenario [30, 32, 33, 34, 35, 36], to differentiate it from the tidal stripping (TS) scenario.

While many studies have addressed the formation and evolution of low-mass dwarf satellites (see ref.[37, 38] and references therein), the formation of the metal-rich CSSs (i.e. apparent outliers in the mass-metallicity relation in the $10^8 - 10^{10} M_\odot$ mass range) has not been studied in a cosmological context. In this work we quantitatively assess the relative likelihood of different formation pathways of metal-rich CSSs (most are cEs) using a large-volume cosmological simulation.

Two Formation Channels of Metal-Rich CSSs in TNG50

We identify 227 metal-rich CSSs at $z = 0$ in the TNG50 simulation [44, 45], which are $\sim 3\sigma$ or $\gtrsim 2\sigma$ outliers above the stellar mass-metallicity relation typical of ordinary dwarf galaxies, as shown by Figure 1 (triangles), using selection criteria based on ref.[12, 13, 14, 46] (see Methods). We then track the evolution of these CSSs on the stellar mass-metallicity ($M_* - \langle [Z/H] \rangle$) plane over time (individual thin trajectories in Figure 1). We thus categorize them into two distinct types based on whether they reach the peak mass on the CSS track or remain below it: Bursty star formation-dominated CSSs (BSF-CSSs, blue triangles, accounting for $173/227 \simeq 76\%$) that quickly evolve to higher masses and metallicities before experiencing a moderate decrease in mass, and tidal stripping-dominated CSSs (TS-CSSs, red triangles, accounting for $54/227 \simeq 24\%$) that reach high metallicity on the $M_* - \langle [Z/H] \rangle$ plane, where metallicity increases as tidal stripping substantially reduces their mass.

We have confirmed that all CSSs selected based on our criteria are satellite galaxies, primarily associated with massive host galaxies. The majority (60-80%) of these CSSs are found within $0.1 R_{\text{vir}}$ of their host halos, but formed outside $2r_e^{\text{host}}$ of their host galaxies, as illustrated in Panel **a** of Figure 2. Panel **b** shows that all these CSSs have significantly more massive hosts, with an average halo mass of $\sim 10^{13} M_\odot$. This is consistent with the observation (e.g. ref.[12, 13, 47]) that CSSs are often associated with massive galaxies. We identify the host galaxies as the most massive neighbour, confirming in most cases that the CSS orbits its putative host. There are also 31 CSSs orbiting around larger satellite galaxies themselves orbiting more massive galaxies.

In general, BSF-CSSs experience their first pericentric passage later than TS-CSSs, suggesting more rapid transformations (Panel **c**). In Panel **d**, we show the probability that any given central galaxy in TNG50 hosts at least one satellite CSS. Approximately half of M31-mass galaxies host at least one CSS, in contrast to around 20% of MW-mass galaxy hosts. Panel **e** examines how the average number

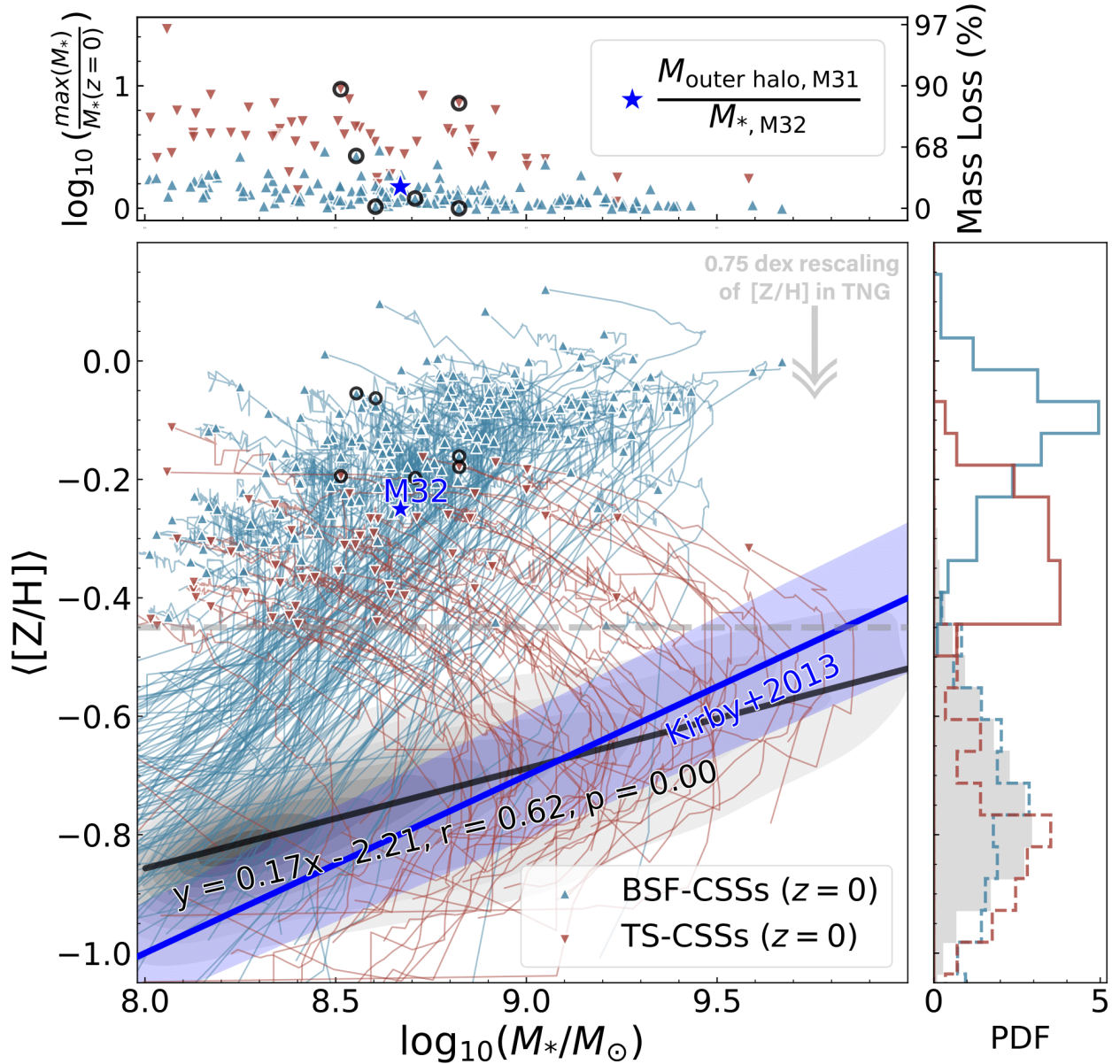


Figure 1: **Evolution of CSSs on the Stellar Mass-Metallicity Diagram and Their Classification.** Thin trajectories represent individual galaxies that end up in the region of CSSs. The CSSs selected according to our criteria at $z = 0$ in TNG50 can be classified as BSF-CSSs (blue triangles) or TS-CSSs (red triangles). The black solid line represents the fitted data for ordinary dwarf galaxies in TNG50. The grey arrow in the upper right corner of the main panel indicates the uniform 0.75 dex rescaling we apply to the metallicities of TNG50 galaxies in this figure, to better align them with the observed scaling relation [39] (refer to Methods for details). We calculate the stellar mass of each CSS within the effective radius, r_e . For comparison, M32 is represented by the blue star. We approximate M32’s mass within r_e based on the total mass from ref.[40]. The selected M32-like CSSs (see Methods) in TNG50 are indicated by black circles. The distribution of ordinary dwarf galaxies at $z = 0$ is plotted with grey shaded region. The adjusted metallicity distributions at $z = 0$ (solid lines) and at the time of the earliest progenitor according to the merger tree (dashed lines), as well as the metallicity distributions of ordinary dwarfs at $z = 0$, are shown as histograms in the right panel. In the top panel, we display the ratio of maximum stellar mass to the mass at $z = 0$ for all CSSs, with the mass loss rate shown on the right-hand axis. The blue star in this panel represents the mass ratio between the outer stellar halo of M31 [27] ($M_{\text{outer halo, M31}}$ and the stellar mass of M32 ($M_{*, \text{M32}}$). Other legends are consistent with the main panel.

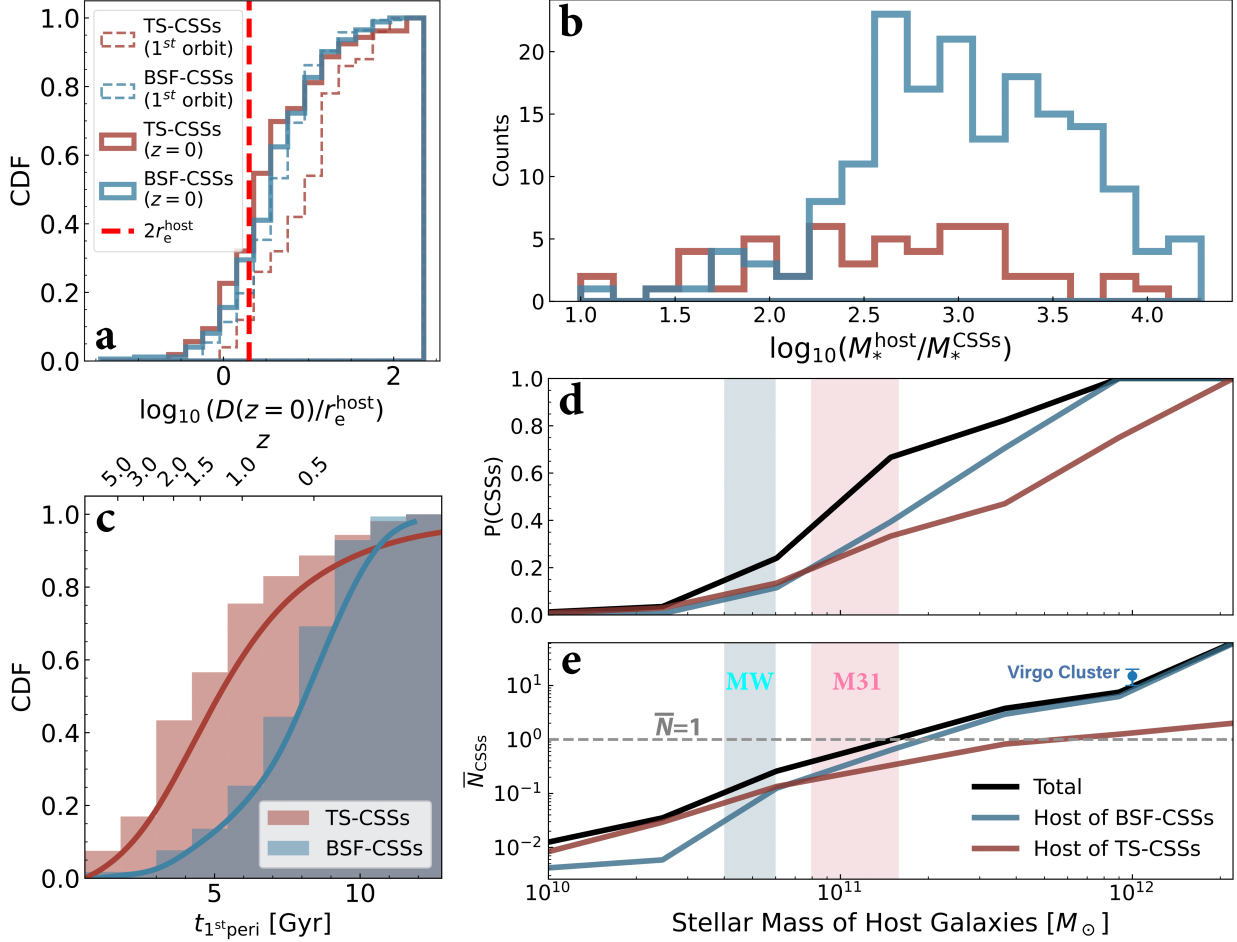


Figure 2: **Panel a.** Normalized distribution of the galactocentric distances of CSSs from their hosts at $z = 0$. The BSF-CSSs are represented in blue, while the TS-CSSs are depicted in red. Dashed histograms show the median distance of each CSSs from its host galaxy during the first orbit. **Panel b.** The mass ratio of CSSs to their host galaxies' stellar mass at $z = 0$ in TNG50. CSSs selected based on our criteria are exclusively found near massive host galaxies. **Panel c.** The cumulative distribution function of the time of the first pericentric passage for BSF-CSSs and TS-CSSs. **Panel d.** The probability of central galaxies hosting CSSs in TNG50. The black solid line displays the ratio between the number of central galaxies having at least one CSS satellite of $M_* = 10^8 - 10^{10} M_\odot$ and the number of all central galaxies at a given stellar mass. We indicate the stellar mass at $z = 0$ of the MW (in cyan, based on ref.[41] and M31 (pink, from ref.[42, 43]). **Panel e.** The average number of CSSs as a function of the stellar mass of their host galaxies. The number of CSSs hosted by galaxies with a mass around $10^{12} M_\odot$ in the Virgo cluster is indicated by the blue circles in this panel.

of CSSs varies with the host stellar mass. Over half of the CSSs in our sample are hosted by galaxies with stellar masses exceeding M_{31} . It can be seen that a galaxy of stellar mass $\gtrsim 10^{12} M_{\odot}$ hosts over 10 CSSs on average, in agreement with observations in the Virgo cluster [48]. Combining Panels **d** and **e**, it becomes clear that if tidal stripping were the only mechanism involved (represented by the red line), the frequency of CSSs would be too low at the high mass end; for instance, in the Virgo cluster, there are 10 – 20 CSSs hosted by galaxies with $M_* \simeq 10^{12} M_{\odot}$ [48], a number consistent with the CSS predictions (black line) from TNG, while the tidal stripping prediction would be just for over one CSS for galaxies with masses larger than $10^{12} M_{\odot}$.

Differences in Evolutionary Pathways

In Panels **A** to **F** and **a** to **f** of Figure 3, we present the evolution of several physical properties of CSSs, distinguishing between two formation mechanisms. We identified four M32-like CSSs dominated by BSF and two dominated by TS, represented by the colored lines in Figure 3. The orbits and morphology of two typical CSSs are shown in the bottom panels. The SFR in BSF-CSSs increases significantly during the first pericentric passage (Panel **a** of Figure 3). These star formation bursts generally last $\lesssim 1$ Gyr, yet lead to dramatic changes in the stellar mass content, morphology, and chemical composition of the CSSs. In comparison, TS-CSSs exhibit less bursty SFRs during their first pericentric passage (see Panel **g**). While BSF-CSSs assemble their mass later (see Panel **c** of Figure 2), fractionally their mass grows more rapidly during their first pericentric passage compared to TS-CSSs (see Panels **B** and **b** of Figure 3). In addition, while TS-CSSs lose between 60%-90% of their peak stellar mass by $z = 0$, BSF-CSSs retain more than half of their peak stellar mass. The gas mass, M_{gas} , and effective radius, r_e , of BSF-CSSs also decrease faster (Panels **C** and **D** of Figure 3), indicating rapid morphological transformation. As shown by the inset images in Panels **G** and **H** of Figure 3 from $t = 7.31$ Gyr (purple star) to $t = 7.61$ Gyr (yellow star), high-density gas clouds collapse, enhancing the stellar density in the central region. Instead, TS-CSSs undergo slow morphological transformations, requiring multiple pericentric passages to lose substantial mass, as illustrated by Panels **g** and **h** of Figure 3. For BSF-CSSs, the metallicity of the gas increases by 1 dex, and that of the stars by 0.8 dex, as shown by Panels **E** and **F**, while the gas metallicity of TS-CSSs does not increase significantly during the first pericentric passage (Panel **e**). Additionally, it is clear that the increase in stellar metallicity is much slower for TS-CSSs (Panel **f**).

Metal Enrichment Caused by Ram Pressure Confinement

We use two M32-like CSSs, a BSF-CSS and the other a TS-CSS, to illustrate the chemo-dynamic evolution during their first pericentric passage. Figures 4 and S.5 show the metal enrichment resulting from ram pressure confinement, evident in the gas's pressure (top), temperature (second), metallicity (third), and 'zoom-in' density (bottom) distributions during the first pericentric passage. We orient the galaxies such that their velocity (the white arrows) is along the y -axis. Their morphology is characteristic of 'jellyfish galaxies', which display long trailing gas tails [49, 50]. In each case, a clear bow shock [51] appears ahead of the galaxy due to its supersonic velocity. The high ram pressure, resulting from the CSSs' rapid motion near the halo center, contributes to triggering bursty star formation by compressing the gas [52]. The bow shock confines some of the metal-enriched hot gas from the bursty star formation to the vicinity of the galaxy for ~ 500 Myr, where it can be recycled into the next generations of stars enabling them to rapidly reach high metallicity. The confined gases extend the duration of bursty star formation in the central regions, thereby helping to rapidly transform a metal-poor but gas-rich dwarf galaxy into a metal-rich CSS, as seen in Panel **F** of Figure 3. A direct comparison between the strength of ram pressure and outflow winds around CSSs (see Methods for details) verifies that ram pressure is able to effectively suppress outflows. For the TS-CSS in Figure S.5, we find that the ram pressure confinement plays a minor role in metal enrichment due to the fact that the progenitors of these CSSs typically are more massive galaxies ($M_* > 10^9 M_{\odot}$), which already host comparatively metal-rich populations at their centers by the time of their first pericentric

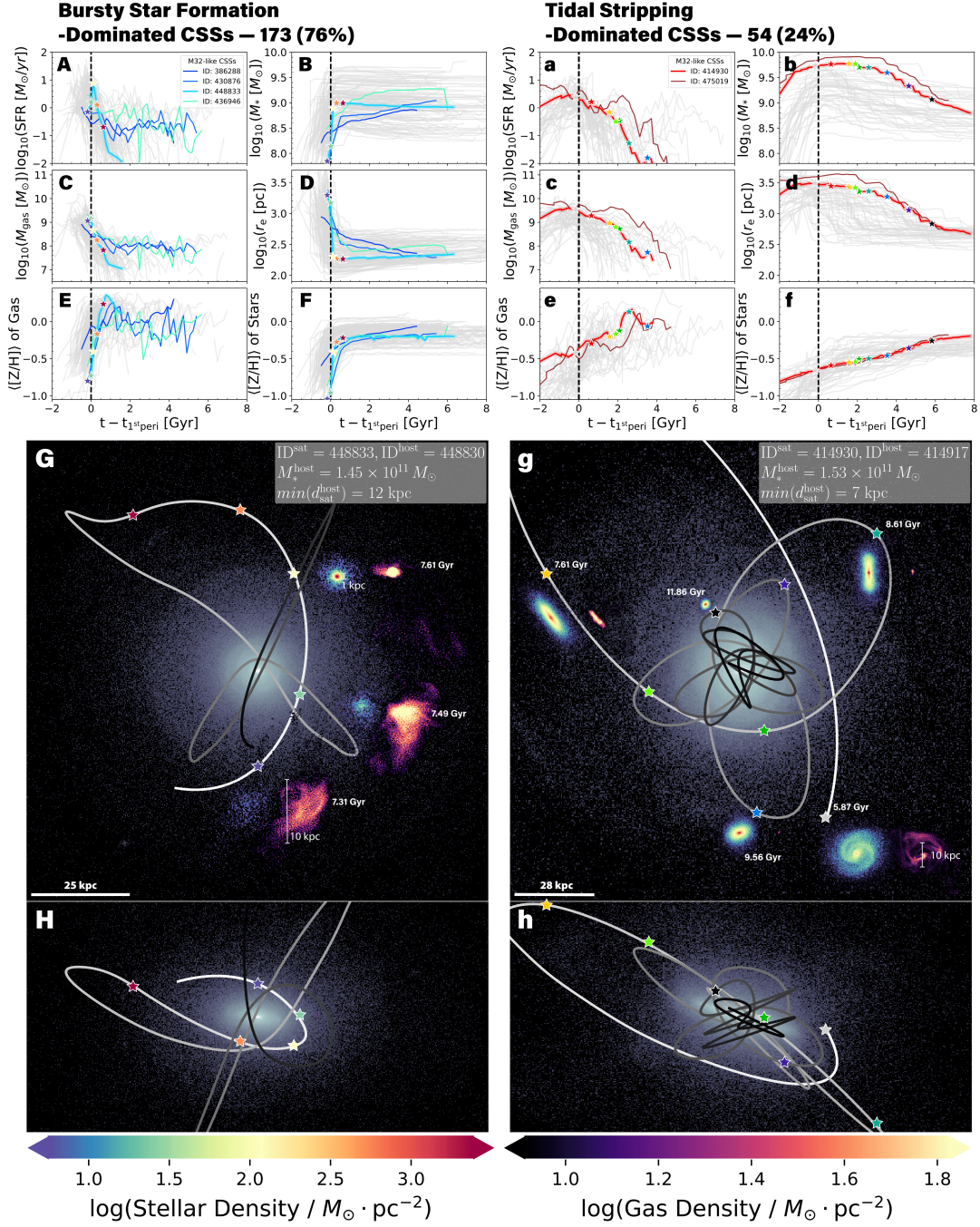


Figure 3: **Upper Panels:** The evolutionary pathways of BSF-CSSs (left, Panels A-F) and TS-CSSs (right, Panels a-f). Panels A-F/a-f show the evolution, centering at the time of the first pericenter ($t_{1^{\text{st}}\text{peri}}$). M_{gas} is the gas mass. The $\langle [Z/H] \rangle$ values of gas and stars represent the mass-weighted average metallicities of star-forming gaseous cells and star particles, respectively. Thin curves represent individual galaxies. The colored lines represent M32-like CSSs. **Lower Panels:** The orbits and stellar and gaseous surface density maps of examples of a BSF-CSS (left, ID 448833, Panels G-H) and a TS-CSS (right, ID 414930, Panels g-h). Interpolation is used to reconstruct the orbits, with a darker color indicating a later time. The colored star symbols mark the positions in their evolution pathways. The background shows the stellar mass surface density distribution of the host galaxy, shown in both face-on (upper) and edge-on (lower) projections at $z = 0$. The inset images, showing the stellar and gas mass surface density distribution of the CSS, are overlaid onto the background images in the face-on views. Panel G presents these maps at three distinct time points, and Panel g at five. For better visibility, the stellar and gas maps are projected at a different spatial scale of 15 kpc by 15 kpc centered on the CSS. For each time, the stellar and gas maps are horizontally offset from each other. At the upper-right corner of Panel G/g, we list the ID for the CSS (ID^{sat}) and the host galaxy (ID^{host}), along with the stellar mass of the host galaxy (M_{*}^{host}), and the minimum distance to the host $\min(d_{\text{sat}}^{\text{host}})$.

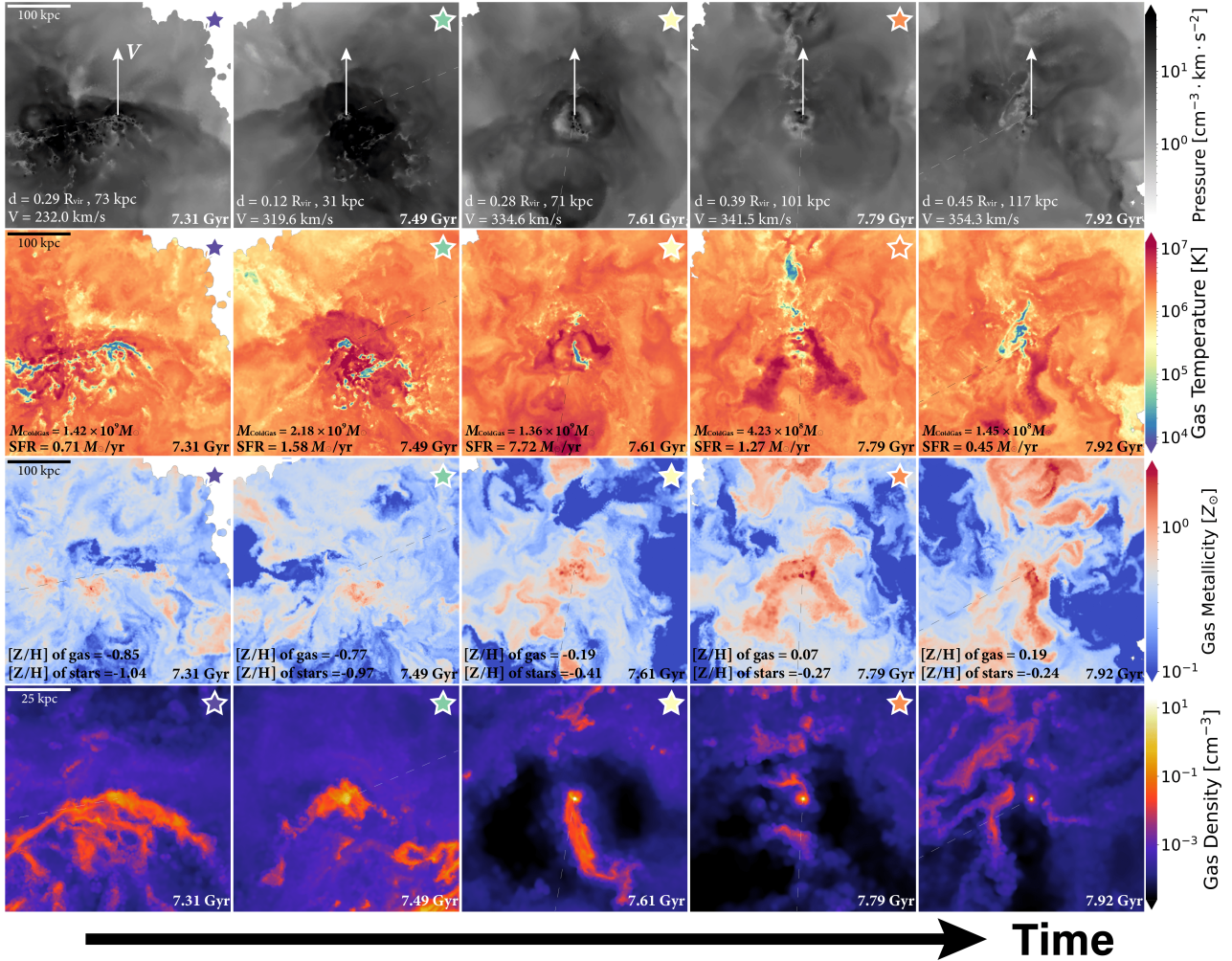


Figure 4: **Illustrative evolution of the gas for a BSF-CSS during the first pericentric passage.** The ID of the CSS at $z = 0$ is 448833. The CSS is centrally positioned within each image, with time annotated on the bottom right corner. Each image (except for those in the bottom row) covers an area of $400 \times 400 \text{ kpc}^2$, projected onto a plane perpendicular to the velocity direction of the CSS, and rendered at a resolution of 800×800 pixels. Dashed lines connect the position of the CSS to its host, while arrows denote the velocity direction of the CSS relative to the host. The top row shows the pressure field, measured in dynes per square centimeter, with distance and velocity indicated in the bottom left corner of each panel. The second row presents the gas temperature, with the mass of cold gas (identified by a star formation rate of the cell > 0) and the SFR shown in the bottom left corner of each panel. The third row shows the evolution of gas metallicity, with the $\langle [Z/H] \rangle$ value of stars and $\langle [Z/H] \rangle$ value of gas specified in the bottom left corner of each panel. The bottom row zooms in on the gas density distribution.

passage. In this dense environment, the strangulation effect [53] and high thermal pressure [54] near a massive galaxy may also contribute to metal enrichment, but less significantly than ram pressure.

Stellar Population Diagnostics of the Two Formation Channels Stellar populations can be used to differentiate between the two formation channels. The top panels of Figure 5, show three example chemical maps of isolated dwarf galaxies. In these galaxies, old stars (pink color) have low metallicity and high α -abundance, while younger stars (dark blue color) have higher metallicity but lower α -abundance. This trend arises from the less intense star formation at late times. The chemical composition of BSF-CSSs, however, exhibits the finger features predicted by ref.[30], as can be seen in the bottom row of upper panels of Figure 5. The generation of these structures is a result of the bursty star formation and rapid enrichment during the first pericentric passage (yellow regions in the lower panels) of CSSs.

The finger features are common in BSF-CSSs (135/173) while 6/54 of TS-CSSs also have similar finger features (see one example in the middle panel of the second row of Figure 5), implying that ram pressure confinement also influences the formation of new stars in the central regions of some TS-CSSs. Although these finger features have been found in very different simulated galaxies – the current work, and ref.[30] – they have not yet been definitively observed in galaxies including M32 due to current observational limitations. Detailed $[\alpha/\text{Fe}]$ ratio measurements are only feasible in the Milky Way and a few nearby galaxies, where spectral data of individual stars can be obtained with sufficient quality. However, exploring similar features in more distant galaxies such as M32 awaits the advanced capabilities of instruments like ELT/*JWST*. We predict that objects affected by ram pressure confinement will exhibit finger features, with stars concentrated in regions of intense star formation. During their formation period, metallicity and $[\alpha/\text{Fe}]$ rise rapidly due to Type II supernovae, but decrease when Type Ia supernovae begin after a few hundred Myr. This would create an age sequence in the finger features, with stars getting younger from the base to the tip, as shown in the bottom row of upper panels of Figure 5.

Another distinctive difference between the two types of CSSs is the scarcity of old stars in BSF-CSSs, due to their relatively late formation, as can be seen in Figure S.6. Conversely, TS-CSSs exhibit a significantly reduced population of young stars compared to isolated dwarfs, a consequence of ram-pressure stripping (RPS) occurring earlier in their histories, as illustrated in Panel **c** of Figure 2.

Stellar Halo and Giant Streams in a M31-M32 Analog System in TNG50 In TNG50, TS-CSSs undergo slow morphological transformations due to multiple events that lead to significant mass loss, as illustrated in the Panels **g** and **h** of Figure 3 and further supported by Figure S.3, contrary to previous models (e.g. ref.[28]), which suggest M32 formed rapidly due to a single tidal interaction ~ 2 Gyr ago, which also resulted in M31’s giant stream.

We identified a fairly realistic M31-M32 analog system (ID 475016-ID 475019) shown in Figure 6, where at low redshifts, tidally induced giant stellar streams form, similar to observed structures [55, 56, 57]. These streams, which include material from the host galaxy (shown in blue and green) as well as the tidally stripped debris of the CSS progenitor (shown in yellow and red), phase mix over time. However, the massive CSS progenitor ($M_* \simeq 10^{10} M_\odot$), generates a giant stellar stream from the host galaxy, resulting in a stellar halo of too high a mass, with the outer halo ($R > 30$ kpc) having a mass of $2.98 \times 10^{10} M_\odot$ at $z = 0$, whereas observations of M31 suggest a total stellar halo mass of $\simeq 2.1_{-0.4}^{+1.7} \times 10^9 M_\odot$ [26]. This discrepancy suggests that the TS scenario is unlikely to be the cause of M32. We conclude that the BSF scenario offers a more likely explanation for the observed relatively low-mass stellar halo of M31.

Given the absence of a well-defined physical demarcation between UCDs and cEs, it is reasonable to expect similar evolutionary pathways for both populations. This expectation is supported by the analysis of ref.[58]. They identified a subset of CSSs with a stellar mass in the range of $M_* \sim 10^6 - 10^9 M_\odot$ in the high-resolution NewHorizon simulation. They identify some of these objects as

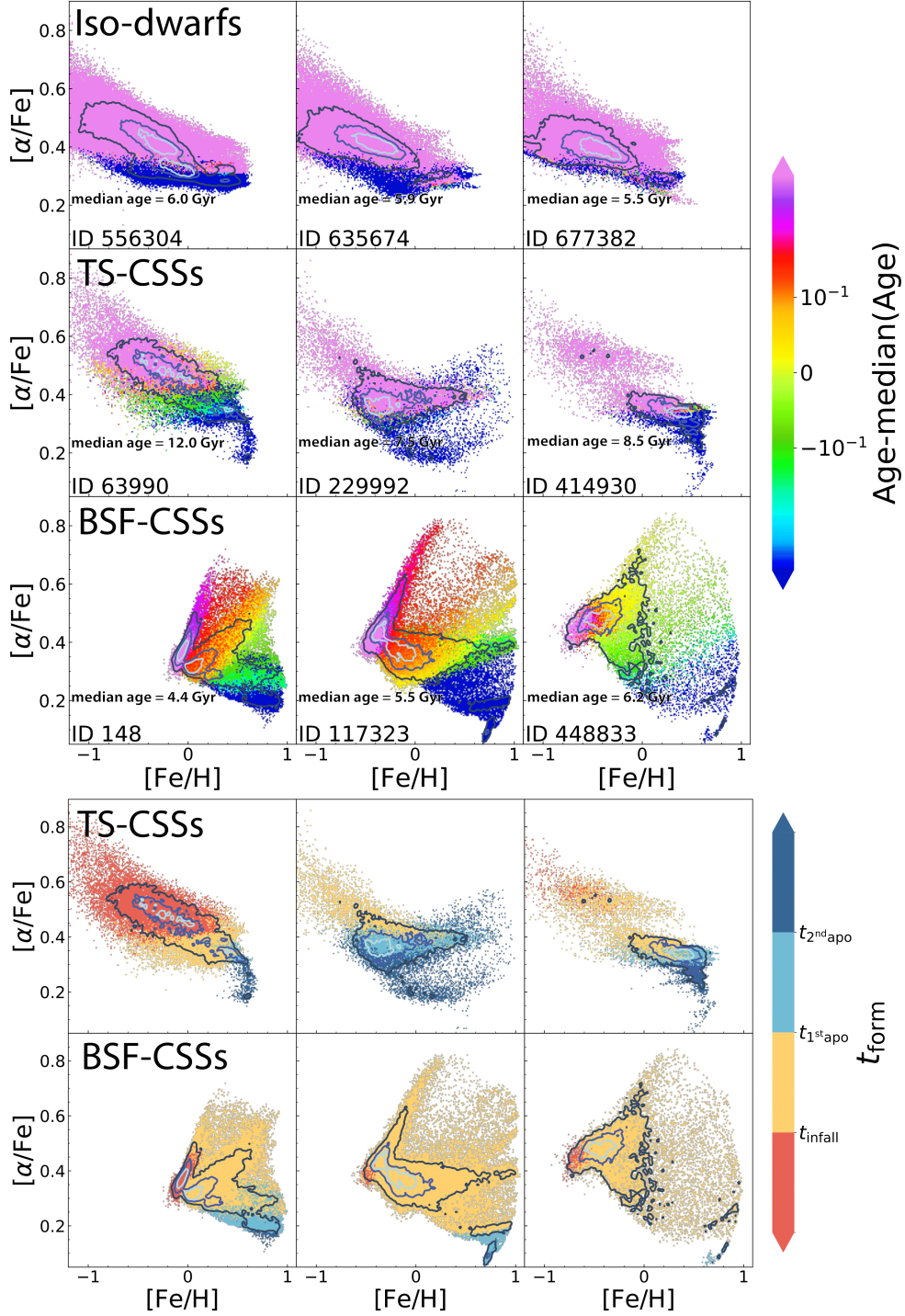


Figure 5: $[\alpha/\text{Fe}]-[\text{Fe}/\text{H}]$ diagram of stellar populations of CSSs at $z = 0$ formed by different mechanisms. α species are ^{12}C , ^{16}O , ^{20}Ne , ^{24}Mg , ^{28}Si . The contours from light to dark blue represent the 20, 40, and 80 percentiles of the maximum density, respectively. In the upper nine panels, from top to bottom, we present cases of isolated central dwarfs (Iso-dwarfs), TS-CSSs, and BSF-CSSs, with stars color-coded based on the difference between their age and the median age of the stellar populations in their respective galaxies. In the lower six panels, stars are color-coded based on their respective formation periods to illustrate the timing of the formation of distinct stellar populations: red (stars formed before infall), orange (during the first orbit), light blue (during the second orbit), and navy (beyond the second orbit). These distributions exhibit significant differences, with BSF-CSSs exhibiting distinct finger features extending towards high $[\alpha/\text{Fe}]$ and $[\text{Fe}/\text{H}]$.

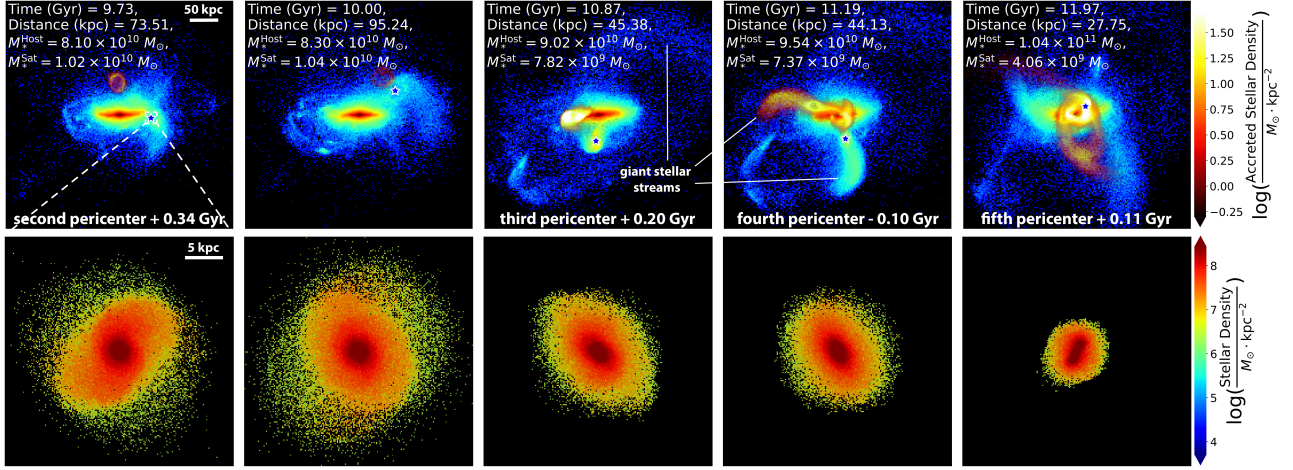


Figure 6: **Formation of the stellar halo in a TS-dominated M31-M32 analog system.** Here we select the time when the CSS is interacting with the central host, resembling the M31-M32 system. The first row shows the stellar halo formed through close interactions. The stellar halo is comprised of material from both the central galaxy (depicted in blue colors) and from the progenitor of the CSS (depicted using a yellow and red colors). The second row’s detailed images display the stellar surface density of the CSS during these interactions.

‘intrinsic-associated’, noting their metal-rich nature and minimal dark matter, which closely aligns with our BSF-CSSs. They indicate that they are a result of a single quick starburst. Notably, the proportion of ‘intrinsic-associated’ to ‘stripped’ CSSs in their study—70%/30%—aligns with our 76%/24% ratio in TNG50, which supports the dominance of the BSF pathway over TS in the formation of UCDs.

Our study, employing a larger sample size, highlights the critical role of ram pressure confinement in dense environments for the formation and evolution of CSSs of a higher mass range ($10^8\text{--}10^{10} M_{\odot}$). Originating from gas-rich dwarf galaxies around $z \sim 1$, these systems undergo rapid transformation due to ram pressure compression and are further shaped by tidal stripping. This compression not only prevents gas outflows but also triggers bursty star formation in satellites close to massive hosts, leading to the emergence of new, metal-rich stellar populations. This agreement of independent studies corroborates the universality of the processes shaping the evolution of CSSs.

Data availability The IllustrisTNG simulations are publicly available at <https://www.tng-project.org/data> [59]. Additional data directly related to this publication are available on request from the corresponding author.

Acknowledgements The authors acknowledge the support by China Manned Space Program through its Space Application System, the Natural Science Foundation of Xiamen China (No. 3502Z202372006), the Fundamental Research Funds for the Central Universities (No. 20720230015), and the Science Fund for Creative Research Groups of the National Science Foundation (NSFC) of China (No. 12221003). L.C.H. is supported by the National Science Foundation of China (11721303, 11991052, 12011540375, 12233001), the National Key R&D Program of China (2022YFF0503401), and the China Manned Space Project (CMS-CSST-2021-A04, CMS-CSST-2021-A06). R.C. is supported in part by the National Key Research and Development Program of China. CG acknowledges support from the National Natural Science Foundation of China (No. 12373007). HL is supported by the National Key R&D Program of China No. 2023YFB3002502, the National Natural Science Foundation of China under No. 12373006. We thank Guangwen Chen and Hongxin Zhang for supplying the literature CSSs data. We thank Volker Springel for helpful discussion. This study utilizes the TNG50 simulation, one of the flagship runs of the IllustrisTNG project, run on the HazelHen Cray XC40 system at the High Performance Computing Center Stuttgart as part of project GCS-ILLU of the Gauss centers for Supercomputing (GCS). The data analysis was conducted using yt (<https://yt-project.org>, [60]), Numpy [61], Scipy [62], Matplotlib [63], Seaborn [64], Pynbody [65], Pandas [66] and h5py [67]. This work was also strongly supported by the Computing Center in Xi'an.

Competing Interests The authors declare that they have no competing interests.

Correspondence Correspondence and requests for materials should be addressed to Min Du (E-mail: du-min@xmu.edu.cn).

Supplementary Material Methods, Supplementary Text, Figures S.1-S.7.

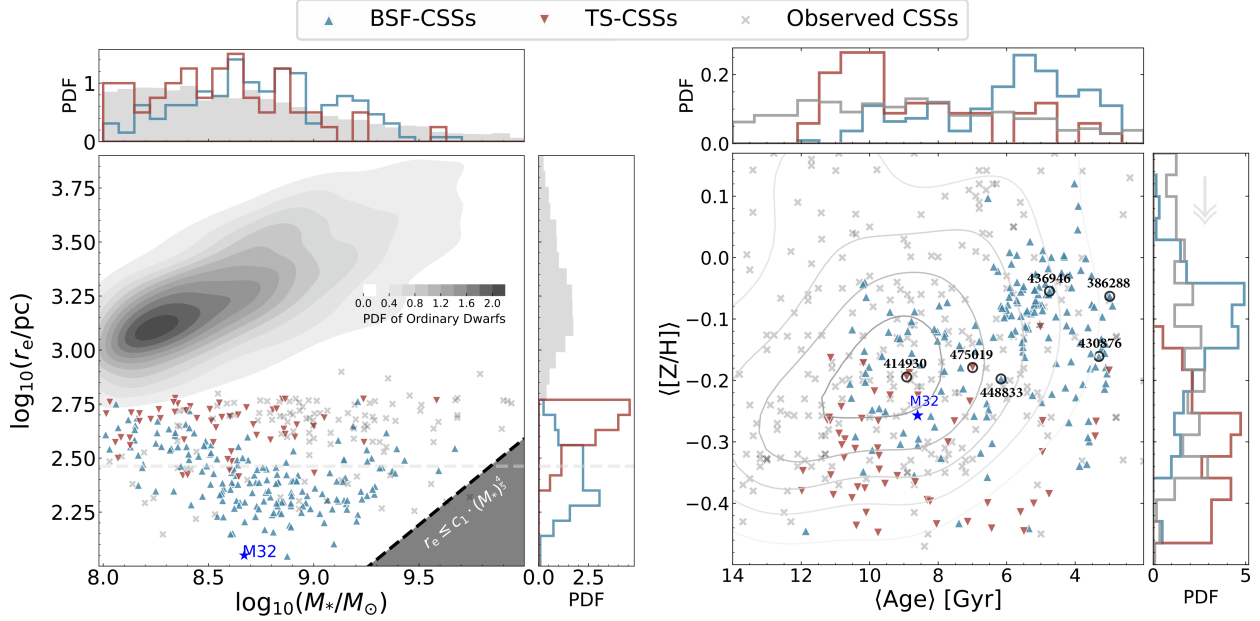


Figure S.1: **Left: The mass–size distribution of CSSs in TNG50 at $z = 0$.** The blue and red triangle markers represent the CSSs in TNG50 selected based on our criteria. Blue triangles denote BSF-CSSs and red triangles represent TS-CSSs. The distribution of ordinary dwarf galaxies is indicated by grey density scale, since they are numerous. Observed CSSs [13, 14, 21, 47, 68] are overlaid using gray crosses. The classifications are described in the text following Figure 1. M32 is represented by a blue star. The black dashed line corresponds to the minimum size limit of stellar systems and the dark grey filled region represents *the zone of avoidance* [$r_e \leq 2.24 \times 10^{-6} \text{pc} \cdot M_\odot^{-4/5} \cdot (M_*)^{4/5}$; see ref. 69, 70, for details]. The light grey dashed line corresponds to a Plummer equivalent gravitational softening length at $z = 0$. In the upper and right sub-panels, M_* and r_e distributions are shown as histograms, as well as that of ordinary dwarf galaxies (grey). **Right: Mass-weighted stellar age versus metallicity of TNG50 CSSs.** The M32-like samples are marked by black circles. Gray contours show the overall distribution of CSSs from observations. The age and shifted metallicity distributions are shown as histograms in the upper and right panels. The grey arrow in the upper corner of the right sub-panel indicates that we apply a uniform 0.75 dex rescaling to the metallicities of TNG50 galaxies, as shown in this figure, to align them with the observational scaling relation [39], as in Figure 1.

Methods

IllustrisTNG The IllustrisTNG Project [71, 72, 73, 74, 75], hereafter TNG, is a suite of magneto-hydrodynamic cosmological simulations run with the moving-mesh code AREPO [76]. The suite encompasses three distinct runs, TNG50, TNG100, and TNG300, characterized by cubic volumes of approximately 50, 100, and 300 Mpc side lengths, respectively. The simulations are run with gravo-magnetohydrodynamics (MHD) and incorporate a comprehensive subgrid model [see 77, 78, for details]. TNG has successfully reproduced many fundamental properties and scaling relations of observed galaxies. In particular, ref.[44] highlights TNG50’s ability to realistically reproduce galactic outflows due to supernovae and black hole feedback. TNG50’s high resolution facilitates detailed studies, with ref.[45] noting the consistency in star-forming galaxy thickness compared to observations. Additionally, the simulated barred galaxies, as detailed in ref.[79], further testify to the reliability of TNG100. TNG galaxies are identified and characterized with the Friends-of-Friends [FoF 80] and SUBFIND [81] algorithms. Halos are dark matter regions containing galaxies and consist of a smooth component and gravitationally bound subhalos. Merger trees for subhalos are constructed using the SubLink algorithm, which identifies descendants through a three-step process based on shared particles and a merit function; the algorithm also addresses undetected subhalos by allowing

snapshot skips and determines the main progenitor based on its mass history [see ref. 82, for details]. Resolution elements (gas, stars, dark matter, and black holes) belonging to an individual galaxy are gravitationally bound to its host subhalo. The adopted cosmology of the TNG project is the Planck 2015 [83], given by: $\Omega_\Lambda = 0.6911$, $\Omega_m = 0.3089$, $\Omega_b = 0.0486$, $\sigma_8 = 0.8159$, $n_s = 0.9667$, and $h = 0.6774$.

The TNG50 Simulation We use the TNG50 [44, 45] (aka TNG50-1) simulation, for its exceptional resolution and statistical significance, making it highly suitable for studying the evolution of dwarf galaxies. TNG50, has 2×2160^3 initial resolution elements (baryon mass of $8 \times 10^4 M_\odot$). Dark matter particles are resolved at masses of $4.5 \times 10^5 M_\odot$. The softening lengths for the collisionless components (dark matter and stars) increase with cosmic time, reaching a physical value of 288 pc at $z = 1$ after starting from 576 comoving pc. The gas softening length begins at 74 comoving pc, with the smallest gas cell size being 8 pc. The median spatial resolution of star-forming ISM gas is $\sim 100 - 140$ pc (from $z = 0$ to $z = 6$). This resolution approaches or exceeds that of modern “zoom-in” simulations of individual massive galaxies, while the volume contains $\sim 20,000$ resolved galaxies with $M_* > 10^7 M_\odot$.

Sample Selection From TNG50, which at $z = 0$ samples thousands of $10^8 - 10^{10} M_\odot$ galaxies, we select the metal-rich CSSs based on their $z = 0$ properties. Our selection criteria do not impose any conditions on their evolution.

We use the selection criteria presented and motivated in ref.[12] and already used by ref.[14] and ref.[46]. To be selected as a metal-rich CSS, a TNG50 galaxy must meet the following three conditions at $z = 0$:

- (A) Compactness: Effective radius $r_e \lesssim 600$ pc.
- (B) Galaxy stellar mass: $M_* = 10^8 - 10^{10} M_\odot$, calculated within r_e .
- (C) Metallicity: Adjusted $\langle [Z/H] \rangle > -0.45$ (Note: The adjustment of $\langle [Z/H] \rangle$ by -0.75 dex to align with observational data is detailed in the subsequent section “Rescaling of Metallicity in The TNG50 Simulation”). This additional condition is aimed at identifying CSSs that deviate from the usual mass-metallicity trend.

We further exclude objects younger than 3 Gyr because their very limited number of old star particles makes it difficult to trace their evolution using only star particles at $z = 0$. The above selection procedures result in a sample of 227 CSSs in the TNG50 simulation. The selected CSSs (triangles in Figure S.1) are outliers from the mass-size relation of ordinary dwarf galaxies (grey contours). These ordinary dwarfs consist of galaxies other than CSSs in the same mass range. The BSF-CSSs (blue triangles) are generally more metal-rich and younger than the TS-CSSs (red triangles). TS-CSSs have metal-rich but older stellar populations, similar to those typically found in high-mass early-type galaxies [10], betraying their genesis within the centres of massive galaxies. These two types of CSSs distribute similarly in mass, while BSF-CSSs are generally more compact than TS-CSSs (left panel of Figure S.1).

Rescaling of Metallicity in The TNG50 Simulation We adopt a solar metallicity value of $Z_\odot = 0.0127$ with solar abundance values for other elements taken from ref.[84]. To align the metallicities of ordinary dwarf galaxies in TNG50 with observational data from ref.[39] for similar mass ranges, we implement a uniform rescaling, applying a downward adjustment of -0.75 dex to the metallicities of all galaxies within the mass range of $10^8 - 10^{10} M_\odot$. Detailed comparisons between TNG50 metallicities and the observational data cited in ref.[39] have not been made, and will need to account

for observational biases and differences in calibration methods, this adjustment serves to make our analyses more comparable overall. Importantly, this rescaling adjusts the absolute values but preserves the relative differences, ensuring that the selected CSSs remain more metal-rich than ordinary dwarfs within the same mass range. Furthermore, as shown in the right panel of Figure S.1, the age-metallicity distribution in TNG50 aligns well with observations post-adjustment, supporting the consistency of our approach.

M31-M32 Analogs in TNG50 In our sample of TNG50 CSSs, we identify 131 galaxies with stellar masses ranging from $10^{8.5}$ to $10^{9.1} M_{\odot}$, similar to that of M32. We then get six M32 analogs located in environments closely resembling the M31-M32 system by restricting the stellar mass of the host galaxies to $M_{*}^{\text{host}} = 10^{10.9} - 10^{11.2} M_{\odot}$ [42, 43]. Their ages and metallicities are highlighted by black circles in the right panel of Figure S.1. Among the six M32-analogs, ID 414930, 448833, and 475019 also have similar ages and metallicities as M32 [85, 86].

Merger Trees of CSSs via Star Particles Matching The standard SubLink algorithm typically relies on dark matter particles to track progenitors. However, this method fails for CSSs due to their low (or even absent) dark matter content. Instead, we used the unique IDs of star particles in each CSS at $z = 0$ to trace back their progenitors across snapshots. Specifically, we identified progenitors by matching star particle IDs from each CSS with those in earlier snapshots, selecting galaxies that hosted the largest number of these particles. This approach allowed us to construct merger trees for 147 CSSs not tracked by the default method, ensuring the evolutionary continuity of our CSS sample. We implement a matching threshold of $10^7 M_{\odot}$, roughly corresponding to 100 star particles, to validate the gravitational association of these particles with their respective galaxies throughout the simulation timeline. Our method effectively identifies progenitors that share significant common star particles with CSSs, offering a robust alternative to traditional dark matter-based tracking.

Identifying CSS Host Galaxies in TNG50 To streamline the identification of CSS host galaxies in TNG50 at $z = 0$, we selected galaxies with stellar masses above $10^9 M_{\odot}$ and used spatial coordinates to conduct a proximity search for potential hosts. We locate the ten nearest neighboring galaxies for each CSS as the potential host. The highest mass galaxy among these neighbors was initially considered as the potential host. If a CSS spent most of its evolution time outside of this galaxy ($D > R_{\text{vir}}$), the next highest mass galaxy was evaluated as a potential host. To enhance the analysis of galaxy trajectories in TNG50, we use cubic spline interpolation to address the simulation’s relatively low temporal resolution. This approach generates a detailed time series, distributed across 1000 uniform points, which significantly improves the resolution of the trajectory plots displayed in Figure S.2. While the majority of CSSs are hosted by central galaxies in TNG50, there are still 31 CSSs whose host galaxies are identified as satellite galaxies of larger mass. The result of this selection process is shown in Panel **b** of Figure 2, illustrating the mass ratio between CSSs and their identified hosts.

Supplementary Text

Paucity of Dark Matter It has been noted that there are CSSs that lack dark matter in different cosmological simulations [58]. They are associated with massive hosts and are relatively metal-rich. The ‘missing dark matter’ in simulations of CSSs suggests that either these systems have formed galaxies with unusually high efficiency or their dark matter content is significantly lower than expected from Λ CDM haloes. Notably, ref.[87] report that the process seen in “jellyfish” galaxies in TNG—where stripped gas in the tails compresses and triggers star formation—could also apply to CSSs. These regions can evolve into self-gravitating dwarf galaxies. Our results suggest that BSF-CSSs are formed from much less massive progenitor galaxies ($\sim 10^{7-8} M_{\odot}$), possibly with smaller dark matter halos than expected, due to enhanced star formation efficiency resulting from close interactions. Furthermore, multiple close interactions with their massive host galaxies result in substantial stripping

of dark matter from the CSSs [88, 89, 90]. Moreover, strong stellar feedback within dwarf galaxies induces significant fluctuations in the gravitational potential by expelling gas, potentially affecting the orbits of dark matter particles and reducing its density [36, 91, 92, 93, 94].

Highly Eccentric Orbits High ram-pressure and bursty star formation are expected to become important when dwarf galaxies reach close proximity to their massive hosts. This is most efficient if the dwarf galaxies are on highly eccentric orbits that bring them close to the host galaxy at high velocities [30, 37, 95]. We compare the orbital characteristics of our CSSs (blue and red histograms) with those of ordinary dwarf galaxies (gray) in Figure S.3. Most CSSs follow orbits with $\epsilon > 0.5$ (the top-left panel), which is determined by the median value of the ratio of the closest and farthest points in their trajectories. Furthermore, CSSs complete more orbits, computed by counting the number of apocenters in their trajectories, compared to ordinary dwarfs, as shown in the top-right panel. In the lower two panels of Figure S.3, it is evident that a significant portion of CSSs undergo high-velocity close interactions with their host galaxies. The median speeds of first pericentric passage $V(1^{\text{st}}\text{orbit}) \simeq 200 - 360$ km/s and the median distances $D(1^{\text{st}}\text{orbit}/R_{\text{vir}}) \simeq 0.15 - 0.31$ during the first orbit. Ram pressure scales as $\rho_{\text{ambient}} v_{\text{bulk}}^2$. CSSs thus experience substantially higher ram pressure compared to ordinary dwarfs. These results are consistent with the predictions in ref.[12] and ref.[30].

Evaluation of Ram Pressure Confinement Effects We assess whether the ram pressure confinement effects can inhibit the winds driven by supernova feedback around the CSSs by comparing the ram pressure, P_{ram} , and the wind pressure, P_{wind} , during the first pericentric passage. As outlined in ref.[96], the ram pressure P_{ram} , is derived as follows:

$$P_{\text{ram}} = \rho_{\text{ambient}} \cdot v_{\text{bulk}}^2 \quad (1)$$

where v_{bulk} is the relative velocity of a galaxy with respect to the surrounding medium. ρ_{ambient} denotes the typical density of the surrounding medium. Here, ρ_{ambient} is calculated as the mean density between R_{vir} and $2R_{\text{vir}}$ around each CSS. The pressure from galactic winds, P_{wind} , is estimated by

$$P_{\text{wind}} = \frac{\dot{M}_{\text{wind}} v_{\text{wind}}}{4\pi R_{\text{M}}^2} = \bar{\rho}_{\text{wind}} \cdot v_{\text{wind}}^2, \quad (2)$$

where \dot{M}_{wind} is the mass outflow rate. We evaluate the effect of ram pressure around the virial radius of CSSs, i.e., $R_{\text{M}} = R_{\text{vir}}$. Note that only gases reaching R_{vir} with $v > v_{\text{esc}}$ can escape the potential well of CSSs. The mass outflow rate is calculated as $\dot{M}_{\text{wind}} = 4\pi R_{\text{M}}^2 \bar{\rho}_{\text{wind}} \cdot v_{\text{wind}}$, where $\bar{\rho}_{\text{wind}}$ represents the mean density of the expelled gases within a shell width $0.01R_{\text{vir}}$ at R_{vir} . v_{wind} is estimated by the mean velocity of gas particles that exceed the local escape velocity. Figure S.4 shows that P_{ram} is generally significantly larger than the wind pressure, P_{wind} . Ram pressure is therefore sufficient to contain outflows during the close approach of CSSs.

Stellar Populations of Each CSS at $z = 0$ Figure S.6 shows all the CSSs in our sample. All BSF-CSSs experienced rapid star formation events, which are primarily accompanied by high [Fe/H] and [α /Fe] in stars compared to Iso-dwarfs. These are consistent with the finger features of BSF-CSSs shown in Figure 5. Their formation was rapid (Myr time scale), as shown in Figure 5 and the lower left panel of Figure S.6. This rapid formation results in BSF-CSSs having a narrower age distribution compared to Iso-dwarfs and TS-CSSs, as illustrated in Figure S.7.

Physical versus Numerical Origins of CSSs Ref.[59] details the classification of subhalos in TNG simulations, distinguishing some subhalos as non-cosmological ‘clumps’ formed from baryonic processes and flagging them for careful analysis, due to their typical characteristics of being low-mass, baryon-dominated, and centrally located in host galaxies at $z < 1$. Ref.[97] further showed that, these so-called ‘clumps’ in TNG50 migrate towards the galaxy center, thereby enhancing the central concentration of stars and gas during mergers or close encounters. In our study, the 147 CSSs not tracked by the default SubLink algorithm correspond to these flagged subhalos. We have extended the

evolutionary history of these objects through star particle matching, capturing their earlier formation periods, and argue for their physical origins and relevance as real CSSs counterparts. Contrary to expectations for mere ‘clumps’ derived from the disks of massive galaxies, which would typically inherit high metallicities at birth, these objects instead exhibit significant subsequent enrichment, as shown in Figure 1. Moreover, the existence of CSSs of even lower mass ($\sim 10^7 M_\odot$) in the `NewHorizon` simulation further corroborates our findings, despite its different numerical methodologies and treatments of stellar feedback.

Numerical Resolution and TNG Model Caveats Ref.[45] argues that the sizes of galaxies with $M_* \gtrsim 10^8 M_\odot$ are reasonably well resolved in TNG50. However, its limited resolution still poses challenges when studying CSSs, potentially affecting these systems. TNG50 uses a Plummer-equivalent gravitational softening length of 0.29 kpc at $z = 0$. This gives a lower limit to the galaxy sizes that can be well resolved, as indicated by the horizontal dashed line in the left panel of Figure S.1, which is greater than the sizes of some of the smallest CSSs in the simulation. Although this softening does not fundamentally skew the gravitational dynamics, it does mean that the gravitational force becomes slightly non-Newtonian below this scale. Given these constraints, our analysis focuses on the overarching, statistically validated characteristics of CSSs. This approach ensures that our conclusions about their formation pathways—reflecting the true physical processes—are robust despite the simulation’s finite resolution.

The simplified ISM model employed in the TNG simulations motivates additional caution [98]. It assumes star formation occurs over a characteristic timescale tied to local dynamical processes such as gas flow, collisions, and compression. Thus star formation rates can vary significantly with environmental conditions. Shorter dynamical times indicate faster gas collapse, potentially leading to rapid star formation, especially in high-density areas. Stellar feedback is implemented through the generation of decoupled kinetic winds, which are proportional to the prompt energy released by SNII explosions [74]. In this regime, the feedback-driven winds exit the ISM of the galaxy without direct interaction, potentially facilitating the artificial formation of compact galaxies. For instance, a more resolved feedback model (e.g. ref.[99]), could disrupt the star-forming ISM of CSSs more effectively or earlier, thereby suppressing their growth. Future simulations with more detailed star formation and stellar feedback models will further illuminate the formation pathways of CSSs.

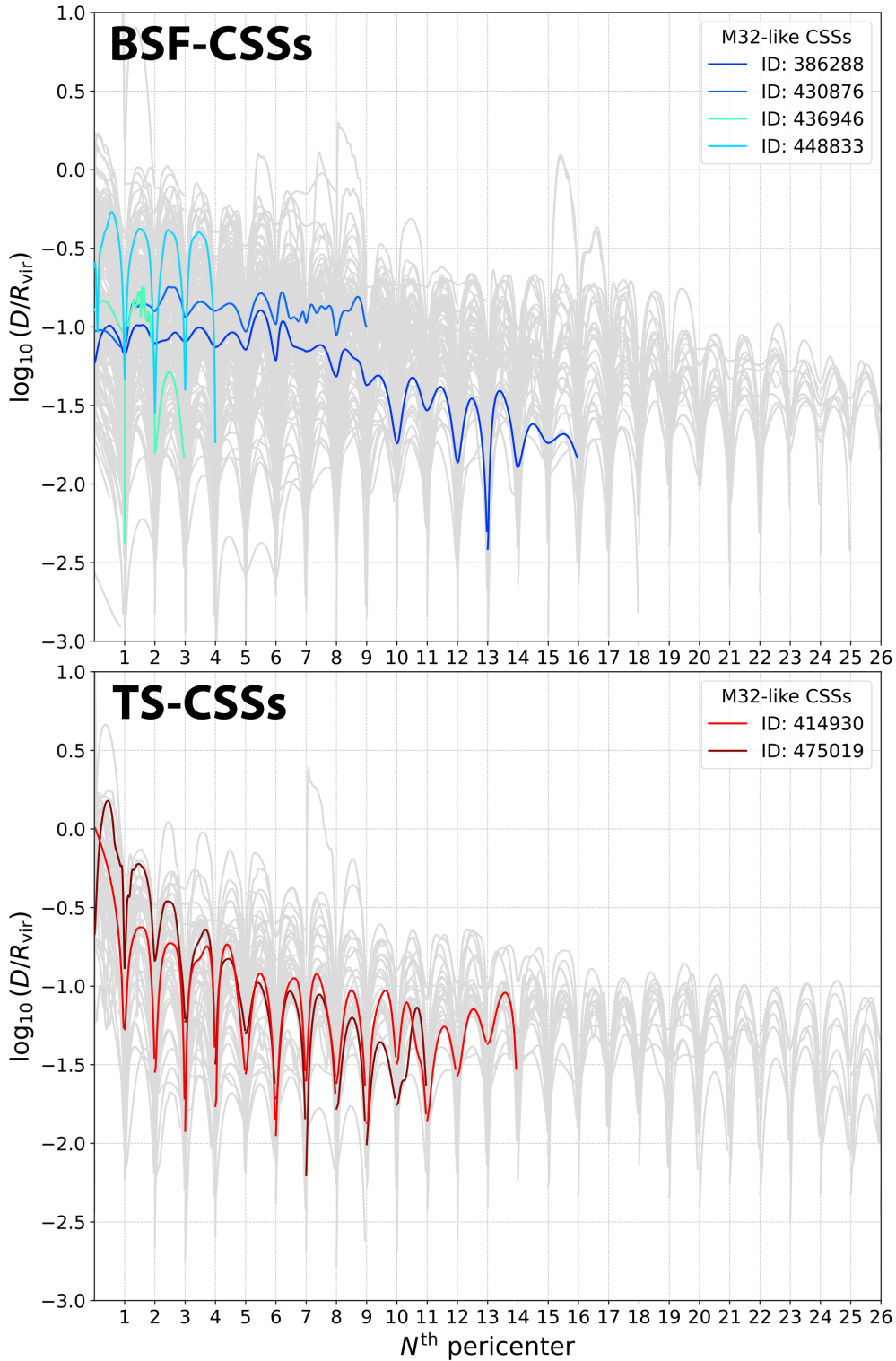


Figure S.2: **Trajectories of CSSs in TNG50.** Thin curves depict individual galaxies, while colored lines represent M32-like CSSs. The figure shows the evolution of distance as a function of number of pericenters for BSF-CSSs (top) and TS-CSSs (bottom). All trajectories have been interpolated using cubic splines.

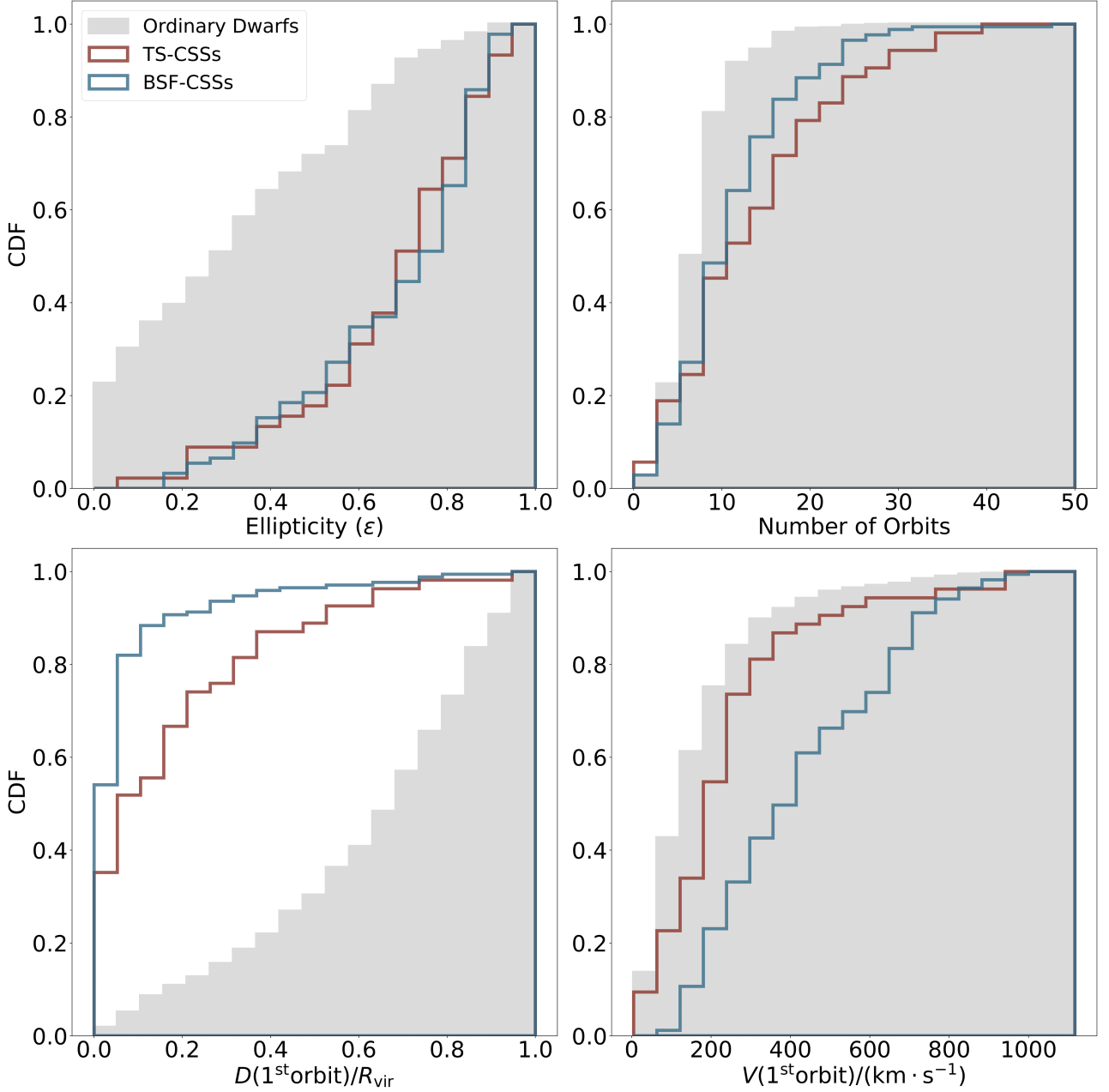


Figure S.3: **The orbital characteristics of CSSs selected based on our criteria in TNG50.** The four panels display CDFs for various orbital characteristics of CSSs, which include ellipticity, number of orbits, the median distance of each galaxy from its host galaxy during the first orbit ($D(1^{\text{st}}\text{orbit})/R_{\text{vir}}$), and the median velocity during the first orbit ($V(1^{\text{st}}\text{orbit})$). The CDFs for BSF-CSSs and TS-CSSs are shown in blue and red, respectively, which allows for a direct comparison against the background distribution of ordinary dwarf galaxies (exclude CSSs), shown in grey. It should be noted that ordinary dwarf galaxies are not necessarily hosted by other galaxies compared to CSSs. The ellipticity, denoted as ϵ , is defined as the median value of $1 - \frac{b}{a}$, where a and b represent the apocenter and pericenter of the orbit, respectively.

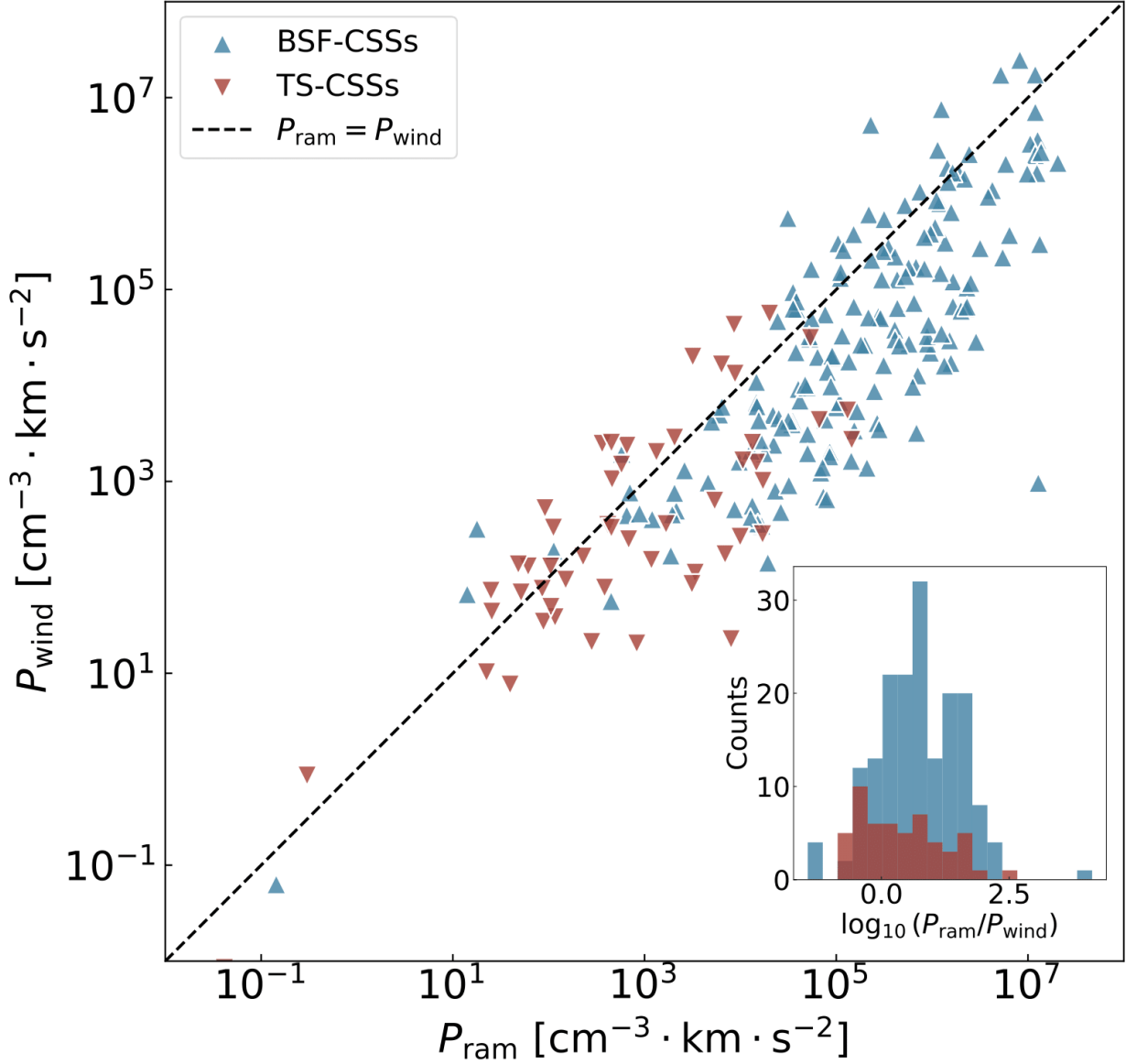


Figure S.4: P_{ram} vs. P_{wind} at R_{vir} of each CSS during its first pericentric passage. The figure compares the ram pressure, P_{ram} , experienced by CSSs as they move through the surrounding medium (defined by Equation 1), with the pressure exerted by galactic winds, P_{wind} , as defined by Equation 2. The data is shown with blue for BSF-CSSs and red for TS-CSSs. The inset image shows the distribution of $\log(P_{\text{ram}}/P_{\text{wind}})$.

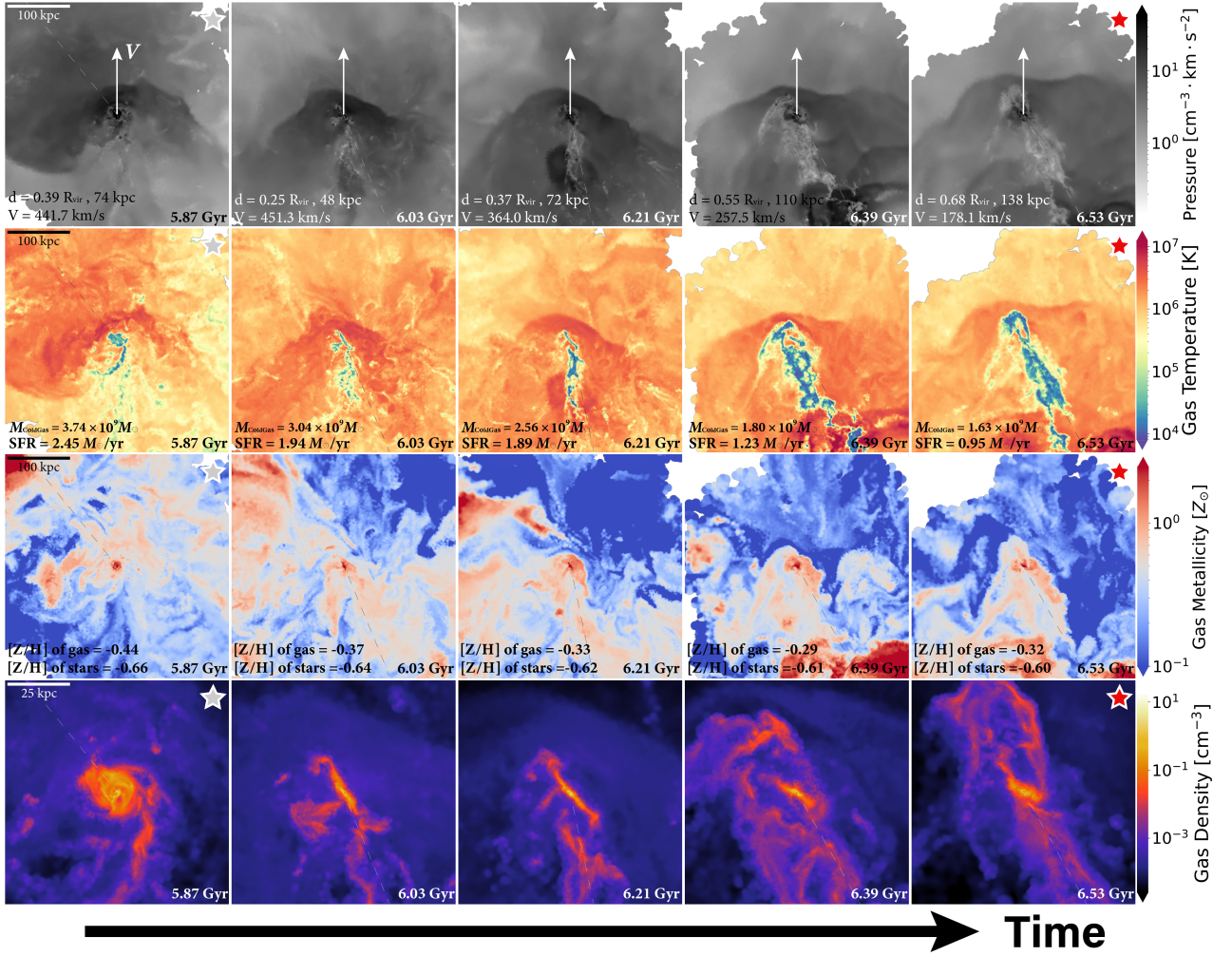


Figure S.5: **Illustrative evolution of the surrounding gas for a TS-CSS during the first pericentric passage.** The ID of the CSS at $z = 0$ is 414930. This figure uses the same conventions as those established in Figure 4.

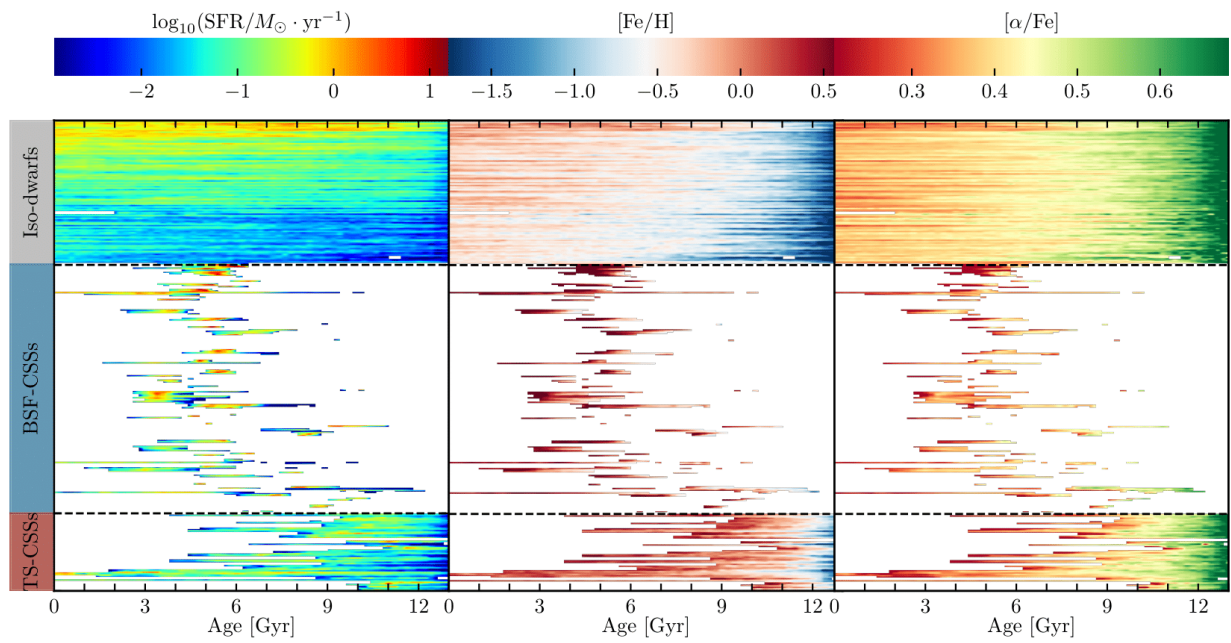


Figure S.6: **The star formation history of each CSS recovered from their stellar population at $z = 0$.** Each row represents a galaxy, with panels from top to bottom displaying 100 randomly selected Iso-dwarfs (top), the BSF-CSSs (middle), and the TS-CSSs (bottom). From left to right, the panels show the SFR, $[\text{Fe}/\text{H}]$, and $[\alpha/\text{Fe}]$.

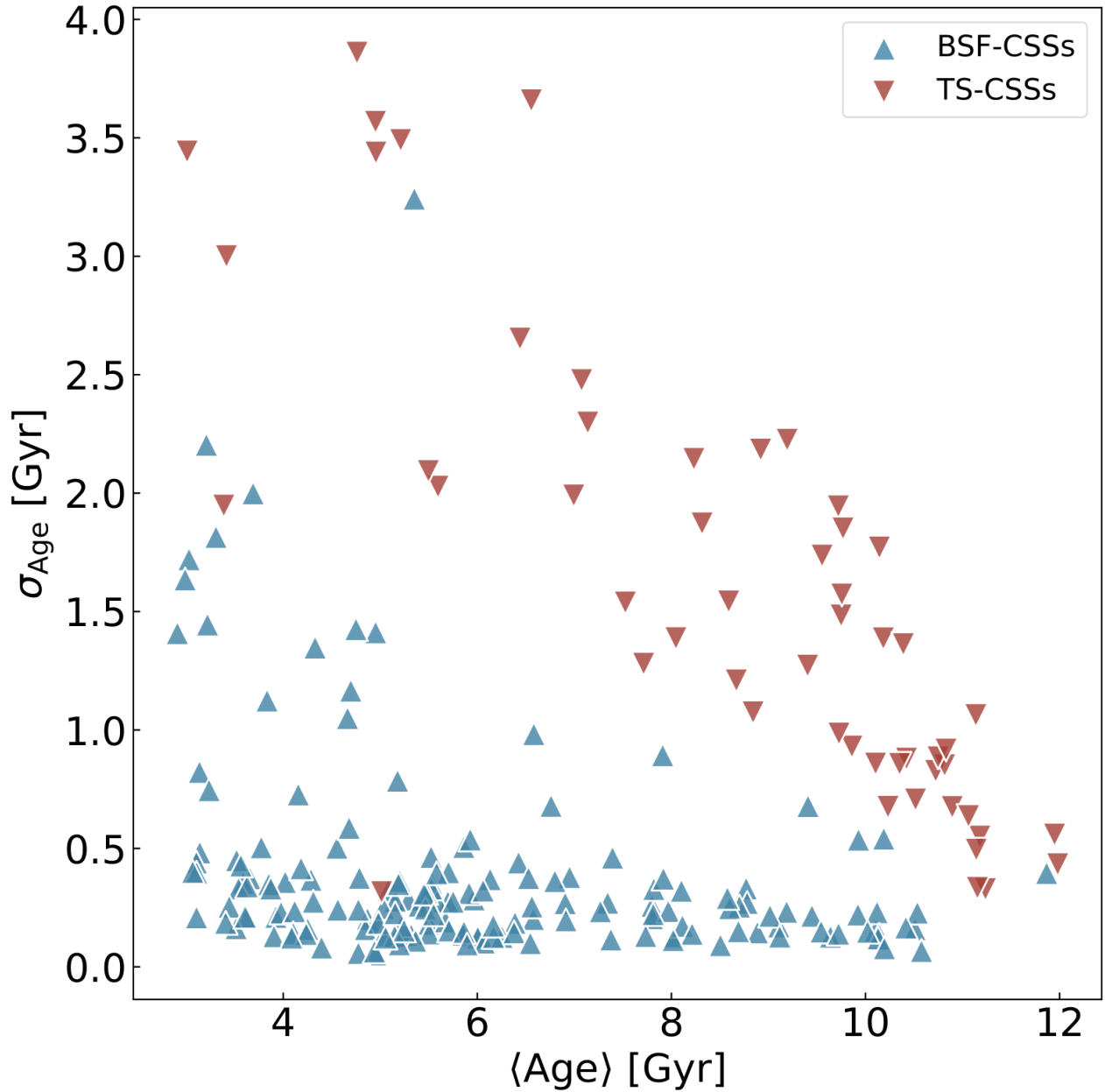


Figure S.7: $\langle \text{Age} \rangle$ vs. σ_{Age} of CSSs. We plot the mass-weighted average age, $\langle \text{Age} \rangle$, versus the age dispersion, σ_{Age} , for each CSS at $z = 0$. Red triangles represent TS-CSSs, while blue triangles represent BSF-CSSs. BSF-CSSs are younger and have a narrower age distribution (typically with $\sigma_{\text{Age}} < 1$ Gyr) compared to TS-CSSs.

1. Drinkwater, M. J. *et al.* Ultra-Compact Dwarf Galaxies in Galaxy Clusters. *Publications of the Astronomical Society of Australia* **21**, 375–378 (2004).
2. Hasegan, M. *et al.* The ACS Virgo Cluster Survey. VII. Resolving the Connection between Globular Clusters and Ultracompact Dwarf Galaxies. *The Astrophysical Journal* **627**, 203–223 (2005). astro-ph/0503566.
3. Jones, J. B. *et al.* Discovery of Ultracompact Dwarf Galaxies in the Virgo Cluster. *The Astrophysical Journal* **131**, 312–324 (2006). astro-ph/0509120.
4. Wehner, E. M. H. & Harris, W. E. Ultracompact Dwarf Candidates in the Hydra Cluster. *The Astrophysical Journal Letters* **668**, L35–L38 (2007). 0708.1514.
5. Misgeld, I., Mieske, S. & Hilker, M. The early-type dwarf galaxy population of the Hydra I cluster. *Astronomy & Astrophysics* **486**, 697–709 (2008). 0806.0621.
6. Mieske, S. *et al.* A search for massive ultra-compact dwarf galaxies in the Centaurus galaxy cluster. *Astronomy & Astrophysics* **498**, 705–710 (2009). 0901.4919.
7. Madrid, J. P. *et al.* Ultra-compact Dwarfs in the Core of the Coma Cluster. *The Astrophysical Journal* **722**, 1707–1715 (2010). 1009.3023.
8. Brodie, J. P., Romanowsky, A. J., Strader, J. & Forbes, D. A. The Relationships among Compact Stellar Systems: A Fresh View of Ultracompact Dwarfs. *The Astronomical Journal* **142**, 199 (2011). 1109.5696.
9. Price, J. *et al.* The HST/ACS Coma Cluster Survey - V. Compact stellar systems in the Coma Cluster. *Monthly Notices of the Royal Astronomical Society* **397**, 1816–1835 (2009). 0906.1123.
10. Chilingarian, I. *et al.* A Population of Compact Elliptical Galaxies Detected with the Virtual Observatory. *Science* **326**, 1379 (2009). 0910.0293.
11. Chilingarian, I. V. & Bergond, G. SDSS J150634.27+013331.6: the second compact elliptical galaxy in the NGC 5846 group. *Monthly Notices of the Royal Astronomical Society* **405**, L11–L15 (2010). 1003.1663.
12. Norris, M. A. *et al.* The AIMSS Project - I. Bridging the star cluster-galaxy divide^{*†‡§¶}. *Monthly Notices of the Royal Astronomical Society* **443**, 1151–1172 (2014). 1406.6065.
13. Janz, J. *et al.* The AIMSS Project - III. The stellar populations of compact stellar systems. *Monthly Notices of the Royal Astronomical Society* **456**, 617–632 (2016). 1511.03264.
14. Kim, S. *et al.* Compact Elliptical Galaxies in Different Local Environments: A Mixture of Galaxies with Different Origins? *The Astrophysical Journal* **903**, 65 (2020). 2008.10686.
15. Gallazzi, A., Charlot, S., Brinchmann, J., White, S. D. M. & Tremonti, C. A. The ages and metallicities of galaxies in the local universe. *Monthly Notices of the Royal Astronomical Society* **362**, 41–58 (2005). astro-ph/0506539.
16. Bekki, K., Couch, W. J. & Drinkwater, M. J. Galaxy Threshing and the Formation of Ultracompact Dwarf Galaxies. *The Astrophysical Journal Letters* **552**, L105–L108 (2001). astro-ph/0106402.
17. Gallazzi, A. R., Pasquali, A., Zibetti, S. & Barbera, F. L. Galaxy evolution across environments as probed by the ages, stellar metallicities, and $[\alpha / \text{Fe}]$ of central and satellite galaxies. *Monthly Notices of the Royal Astronomical Society* **502**, 4457–4478 (2021). 2010.04733.

18. Mayes, R. J. *et al.* Testing the tidal stripping scenario of ultracompact dwarf galaxy formation by using internal properties. *Monthly Notices of the Royal Astronomical Society* **506**, 2459–2470 (2021). 2109.01266.
19. Deeley, S. *et al.* The formation pathways of compact elliptical galaxies. *Monthly Notices of the Royal Astronomical Society* **525**, 1192–1209 (2023). 2308.00305.
20. Huxor, A. P., Phillipps, S., Price, J. & Harniman, R. Tidal streams in newly discovered M32 analogues: evidence for the stripping scenario. *Monthly Notices of the Royal Astronomical Society* **414**, 3557–3565 (2011). 1103.1257.
21. Chilingarian, I. & Zolotukhin, I. Isolated compact elliptical galaxies: Stellar systems that ran away. *Science* **348**, 418–421 (2015). 1504.06990.
22. Wang, K. *et al.* An evolutionary continuum from nucleated dwarf galaxies to star clusters. *Nature* **623**, 296–300 (2023). 2311.05448.
23. McDermid, R. M. *et al.* The ATLAS^{3D} Project - XXX. Star formation histories and stellar population scaling relations of early-type galaxies. *Monthly Notices of the Royal Astronomical Society* **448**, 3484–3513 (2015). 1501.03723.
24. Ibata, R. *et al.* The Haunted Halos of Andromeda and Triangulum: A Panorama of Galaxy Formation in Action. *The Astrophysical Journal* **671**, 1591–1623 (2007). 0704.1318.
25. Courteau, S. *et al.* The Luminosity Profile and Structural Parameters of the Andromeda Galaxy. *The Astrophysical Journal* **739**, 20 (2011). 1106.3564.
26. Williams, B. F. *et al.* The Panchromatic Hubble Andromeda Treasury. II. Tracing the Inner M31 Halo with Blue Horizontal Branch Stars. *The Astrophysical Journal* **759**, 46 (2012). 1209.2416.
27. Gilbert, K. M. *et al.* Global Properties of M31’s Stellar Halo from the SPLASH Survey. I. Surface Brightness Profile. *The Astrophysical Journal* **760**, 76 (2012). 1210.3362.
28. D’Souza, R. & Bell, E. F. The Andromeda galaxy’s most important merger about 2 billion years ago as M32’s likely progenitor. *Nature Astronomy* **2**, 737–743 (2018). 1807.08819.
29. Graham, A. W. Evidence for an Outer Disk in the Prototype “Compact Elliptical” Galaxy M32. *The Astrophysical Journal Letters* **568**, L13–L17 (2002). astro-ph/0202307.
30. Du, M. *et al.* The Formation of Compact Elliptical Galaxies in the Vicinity of a Massive Galaxy: The Role of Ram-pressure Confinement. *The Astrophysical Journal* **875**, 58 (2019). 1811.06778.
31. Williamson, D. & Martel, H. Chemodynamics of Dwarf Galaxies under Ram Pressure. *The Astrophysical Journal* **867**, 72 (2018). 1809.03760.
32. Stinson, G. S., Dalcanton, J. J., Quinn, T., Kaufmann, T. & Wadsley, J. Breathing in Low-Mass Galaxies: A Study of Episodic Star Formation. *The Astrophysical Journal* **667**, 170–175 (2007). 0705.4494.
33. Di Cintio, A. *et al.* The dependence of dark matter profiles on the stellar-to-halo mass ratio: a prediction for cusps versus cores. *Monthly Notices of the Royal Astronomical Society* **437**, 415–423 (2014). 1306.0898.
34. Sparre, M. *et al.* (Star)bursts of FIRE: observational signatures of bursty star formation in galaxies. *Monthly Notices of the Royal Astronomical Society* **466**, 88–104 (2017). 1510.03869.

35. Bose, S. *et al.* No cores in dark matter-dominated dwarf galaxies with bursty star formation histories. *Monthly Notices of the Royal Astronomical Society* **486**, 4790–4804 (2019). 1810.03635.
36. Sales, L. V., Wetzel, A. & Fattahi, A. Baryonic solutions and challenges for cosmological models of dwarf galaxies. *Nature Astronomy* **6**, 897–910 (2022). 2206.05295.
37. Mayer, L. Environmental Mechanisms Shaping the Nature of Dwarf Spheroidal Galaxies: The View of Computer Simulations. *Advances in Astronomy* **2010**, 278434 (2010). 0909.4075.
38. de Almeida, A. P., Mamon, G. A., Dekel, A. & Lima Neto, G. B. What drives the corpulence of galaxies?. I. The formation of central compact dwarf galaxies in TNG50. *Astronomy & Astrophysics* **687**, A131 (2024). 2404.15482.
39. Kirby, E. N. *et al.* The Universal Stellar Mass-Stellar Metallicity Relation for Dwarf Galaxies. *The Astrophysical Journal* **779**, 102 (2013). 1310.0814.
40. Kormendy, J. & Ho, L. C. Coevolution (Or Not) of Supermassive Black Holes and Host Galaxies. *Annual Review of Astronomy and Astrophysics* **51**, 511–653 (2013). 1304.7762.
41. Bland-Hawthorn, J. & Gerhard, O. The Galaxy in Context: Structural, Kinematic, and Integrated Properties. *Annual Review of Astronomy and Astrophysics* **54**, 529–596 (2016). 1602.07702.
42. Tamm, A., Tempel, E., Tenjes, P., Tihhonova, O. & Tuvikene, T. Stellar mass map and dark matter distribution in M 31. *Astronomy & Astrophysics* **546**, A4 (2012). 1208.5712.
43. Sick, J. *et al.* Andromeda (M31) Optical and Infrared Disk Survey. I. Insights in Wide-field Near-IR Surface Photometry. *The Astronomical Journal* **147**, 109 (2014). 1303.6290.
44. Nelson, D. *et al.* First results from the TNG50 simulation: galactic outflows driven by supernovae and black hole feedback. *Monthly Notices of the Royal Astronomical Society* **490**, 3234–3261 (2019). 1902.05554.
45. Pillepich, A. *et al.* First results from the TNG50 simulation: the evolution of stellar and gaseous discs across cosmic time. *Monthly Notices of the Royal Astronomical Society* **490**, 3196–3233 (2019). 1902.05553.
46. Chen, G. *et al.* Discovery of a Bimodal Environmental Distribution of Compact Ellipticals in the Local Universe. *The Astrophysical Journal Letters* **934**, L35 (2022). 2207.12422.
47. Ferré-Mateu, A., Forbes, D. A., Romanowsky, A. J., Janz, J. & Dixon, C. On the formation mechanisms of compact elliptical galaxies. *Monthly Notices of the Royal Astronomical Society* **473**, 1819–1840 (2018). 1709.07012.
48. Ferrarese, L. *et al.* The Next Generation Virgo Cluster Survey (NGVS). XIV. The Discovery of Low-mass Galaxies and a New Galaxy Catalog in the Core of the Virgo Cluster. *The Astrophysical Journal* **890**, 128 (2020).
49. Rohr, E. *et al.* Jellyfish galaxies with the IllustrisTNG simulations - when, where, and for how long does ram pressure stripping of cold gas occur? *Monthly Notices of the Royal Astronomical Society* **524**, 3502–3525 (2023). 2304.09196.
50. Zinger, E., Joshi, G. D., Pillepich, A., Rohr, E. & Nelson, D. Jellyfish galaxies with the IllustrisTNG simulations - citizen-science results towards large distances, low-mass hosts, and high redshifts. *Monthly Notices of the Royal Astronomical Society* **527**, 8257–8289 (2024). 2304.09202.

51. Yun, K. *et al.* Jellyfish galaxies with the IllustrisTNG simulations - I. Gas-stripping phenomena in the full cosmological context. *Monthly Notices of the Royal Astronomical Society* **483**, 1042–1066 (2019). 1810.00005.
52. Göller, J., Joshi, G. D., Rohr, E., Zinger, E. & Pillepich, A. Jellyfish galaxies with the IllustrisTNG simulations - No enhanced population-wide star formation according to TNG50. *Monthly Notices of the Royal Astronomical Society* **525**, 3551–3570 (2023). 2304.09199.
53. Pasquali, A., Gallazzi, A. & van den Bosch, F. C. The gas-phase metallicity of central and satellite galaxies in the Sloan Digital Sky Survey. *Monthly Notices of the Royal Astronomical Society* **425**, 273–286 (2012). 1206.3458.
54. Petropoulou, V., Vílchez, J. & Iglesias-Páramo, J. Environmental Effects on the Metal Enrichment of Low-mass Galaxies in Nearby Clusters. *The Astrophysical Journal* **749**, 133 (2012). 1202.4164.
55. Ibata, R., Irwin, M., Lewis, G., Ferguson, A. M. N. & Tanvir, N. A giant stream of metal-rich stars in the halo of the galaxy M31. *Nature* **412**, 49–52 (2001). astro-ph/0107090.
56. Ferguson, A. M. N., Irwin, M. J., Ibata, R. A., Lewis, G. F. & Tanvir, N. R. Evidence for Stellar Substructure in the Halo and Outer Disk of M31. *The Astronomical Journal* **124**, 1452–1463 (2002). astro-ph/0205530.
57. Zucker, D. B. *et al.* A New Giant Stellar Structure in the Outer Halo of M31. *The Astrophysical Journal Letters* **612**, L117–L120 (2004). astro-ph/0401098.
58. Jang, J. K. *et al.* Formation Pathways of the Compact Stellar Systems. *The Astrophysical Journal* **969**, 59 (2024). 2405.10195.
59. Nelson, D. *et al.* The IllustrisTNG simulations: public data release. *Computational Astrophysics and Cosmology* **6**, 2 (2019). 1812.05609.
60. Turk, M. J. *et al.* yt: A Multi-code Analysis Toolkit for Astrophysical Simulation Data. *The Astrophysical Journal Supplement Series* **192**, 9 (2011). 1011.3514.
61. Harris, C. R. *et al.* Array programming with NumPy. *Nature* **585**, 357–362 (2020). 2006.10256.
62. Virtanen, P. *et al.* SciPy 1.0: fundamental algorithms for scientific computing in Python. *Nature Methods* **17**, 261–272 (2020). 1907.10121.
63. Hunter, J. D. Matplotlib: A 2D Graphics Environment. *Computing in Science and Engineering* **9**, 90–95 (2007).
64. Waskom, M. seaborn: statistical data visualization. *The Journal of Open Source Software* **6**, 3021 (2021).
65. Pontzen, A., Roškar, R., Stinson, G. & Woods, R. pynbody: N-Body/SPH analysis for python. Astrophysics Source Code Library, record ascl:1305.002 (2013).
66. McKinney, W. Data structures for statistical computing in python. In van der Walt, S. & Millman, J. (eds.) *Proceedings of the 9th Python in Science Conference*, 51 – 56 (2010).
67. Collette, A. *et al.* h5py/h5py: 3.5.0 (2021).

68. Gu  rou, A. *et al.* The Next Generation Virgo Cluster Survey. XII. Stellar Populations and Kinematics of Compact, Low-mass Early-type Galaxies from Gemini GMOS-IFU Spectroscopy. *The Astrophysical Journal* **804**, 70 (2015). 1504.03714.
69. Burstein, D., Bender, R., Faber, S. & Nolthenius, R. Global Relationships Among the Physical Properties of Stellar Systems. *The Astronomical Journal* **114**, 1365 (1997). astro-ph/9707037.
70. Misgeld, I. & Hilker, M. Families of dynamically hot stellar systems over 10 orders of magnitude in mass. *Monthly Notices of the Royal Astronomical Society* **414**, 3699–3710 (2011). 1103.1628.
71. Marinacci, F. *et al.* First results from the IllustrisTNG simulations: radio haloes and magnetic fields. *Monthly Notices of the Royal Astronomical Society* **480**, 5113–5139 (2018). 1707.03396.
72. Naiman, J. P. *et al.* First results from the IllustrisTNG simulations: a tale of two elements - chemical evolution of magnesium and europium. *Monthly Notices of the Royal Astronomical Society* **477**, 1206–1224 (2018). 1707.03401.
73. Nelson, D. *et al.* The abundance, distribution, and physical nature of highly ionized oxygen O VI, O VII, and O VIII in IllustrisTNG. *Monthly Notices of the Royal Astronomical Society* **477**, 450–479 (2018). 1712.00016.
74. Pillepich, A. *et al.* First results from the IllustrisTNG simulations: the stellar mass content of groups and clusters of galaxies. *Monthly Notices of the Royal Astronomical Society* **475**, 648–675 (2018). 1707.03406.
75. Springel, V. *et al.* First results from the IllustrisTNG simulations: matter and galaxy clustering. *Monthly Notices of the Royal Astronomical Society* **475**, 676–698 (2018). 1707.03397.
76. Springel, V. E pur si muove: Galilean-invariant cosmological hydrodynamical simulations on a moving mesh. *Monthly Notices of the Royal Astronomical Society* **401**, 791–851 (2010). 0901.4107.
77. Weinberger, R. *et al.* Simulating galaxy formation with black hole driven thermal and kinetic feedback. *Monthly Notices of the Royal Astronomical Society* **465**, 3291–3308 (2017). 1607.03486.
78. Pillepich, A. *et al.* Simulating galaxy formation with the IllustrisTNG model. *Monthly Notices of the Royal Astronomical Society* **473**, 4077–4106 (2018). 1703.02970.
79. Zhao, D., Du, M., Ho, L. C., Debattista, V. P. & Shi, J. Barred Galaxies in the IllustrisTNG Simulation. *The Astrophysical Journal* **904**, 170 (2020). 2009.06895.
80. Davis, M., Efstathiou, G., Frenk, C. S. & White, S. D. M. The evolution of large-scale structure in a universe dominated by cold dark matter. *The Astrophysical Journal* **292**, 371–394 (1985).
81. Springel, V., White, S. D. M., Tormen, G. & Kauffmann, G. Populating a cluster of galaxies - I. Results at $z=0$. *Monthly Notices of the Royal Astronomical Society* **328**, 726–750 (2001). astro-ph/0012055.
82. Rodriguez-Gomez, V. *et al.* The merger rate of galaxies in the Illustris simulation: a comparison with observations and semi-empirical models. *Monthly Notices of the Royal Astronomical Society* **449**, 49–64 (2015). 1502.01339.
83. Planck Collaboration *et al.* Planck 2015 results. XIII. Cosmological parameters. *Astronomy & Astrophysics* **594**, A13 (2016). 1502.01589.

84. Asplund, M., Grevesse, N., Sauval, A. J. & Scott, P. The Chemical Composition of the Sun. *Annual Review of Astronomy and Astrophysics* **47**, 481–522 (2009). 0909.0948.
85. Sánchez-Blázquez, P., Gorgas, J., Cardiel, N. & González, J. J. Stellar populations of early-type galaxies in different environments. II. Ages and metallicities. *Astronomy & Astrophysics* **457**, 809–821 (2006). astro-ph/0604568.
86. Spolaor, M., Kobayashi, C., Forbes, D. A., Couch, W. J. & Hau, G. K. T. Early-type galaxies at large galactocentric radii - II. Metallicity gradients and the [Z/H]-mass, [α /Fe]-mass relations. *Monthly Notices of the Royal Astronomical Society* **408**, 272–292 (2010). 1006.1698.
87. Lora, V., Smith, R., Fritz, J., Pasquali, A. & Raga, A. C. Dark-matter-free Dwarf Galaxy Formation at the Tips of the Tentacles of Jellyfish Galaxies. *The Astrophysical Journal* **969**, 24 (2024). 2404.05676.
88. Smith Castelli, A. V., Faifer, F. R. & Escudero, C. G. Stellar systems in the direction of the Hickson Compact Group 44. I. Low surface brightness galaxies. *Astronomy & Astrophysics* **596**, A23 (2016). 1609.00224.
89. Hammer, F. *et al.* Orbital Evidences for Dark-matter-free Milky Way Dwarf Spheroidal Galaxies. *The Astrophysical Journal* **892**, 3 (2020). 2002.09493.
90. Keim, M. A. *et al.* Tidal Distortions in NGC1052-DF2 and NGC1052-DF4: Independent Evidence for a Lack of Dark Matter. *The Astrophysical Journal* **935**, 160 (2022). 2109.09778.
91. Navarro, J. F., Eke, V. R. & Frenk, C. S. The cores of dwarf galaxy haloes. *Monthly Notices of the Royal Astronomical Society* **283**, L72–L78 (1996). astro-ph/9610187.
92. Gelato, S. & Sommer-Larsen, J. On DDO 154 and cold dark matter halo profiles. *Monthly Notices of the Royal Astronomical Society* **303**, 321–328 (1999). astro-ph/9806289.
93. Read, J. I. & Gilmore, G. Mass loss from dwarf spheroidal galaxies: the origins of shallow dark matter cores and exponential surface brightness profiles. *Monthly Notices of the Royal Astronomical Society* **356**, 107–124 (2005). astro-ph/0409565.
94. Pontzen, A. & Governato, F. How supernova feedback turns dark matter cusps into cores. *Monthly Notices of the Royal Astronomical Society* **421**, 3464–3471 (2012). 1106.0499.
95. McGaugh, S. S. & Wolf, J. Local Group Dwarf Spheroidals: Correlated Deviations from the Baryonic Tully-Fisher Relation. *The Astrophysical Journal* **722**, 248–261 (2010). 1003.3448.
96. Gunn, J. E. & Gott, I., J. Richard. On the Infall of Matter Into Clusters of Galaxies and Some Effects on Their Evolution. *The Astrophysical Journal* **176**, 1 (1972).
97. Boecker, A. *et al.* The origin of stars in the inner 500 parsecs in TNG50 galaxies. *Monthly Notices of the Royal Astronomical Society* **519**, 5202–5235 (2023). 2301.11942.
98. Springel, V. & Hernquist, L. Cosmological smoothed particle hydrodynamics simulations: a hybrid multiphase model for star formation. *Monthly Notices of the Royal Astronomical Society* **339**, 289–311 (2003). astro-ph/0206393.
99. Smith, M. C. *et al.* Efficient early stellar feedback can suppress galactic outflows by reducing supernova clustering. *Monthly Notices of the Royal Astronomical Society* **506**, 3882–3915 (2021). 2009.11309.